Investigation of the concave curvature effect for an impinging jet flow

P. Aillaud,* L. Y. M. Gicquel, and F. Duchaine
CFD Team, Centre Européen de Recherche et de Formation Avancée en Calcul Scientifique, 42 Avenue Gaspard Coriolis, 31057 Toulouse, France
(Received 13 July 2017; published 27 November 2017)

The concave curvature effect for an impinging jet flow is discussed in this paper. To do so, a submerged axisymmetric isothermal impinging jet at a Reynolds number (based on the nozzle diameter and the bulk velocity at the nozzle outlet) Re = 23 000 and for a nozzle to plate distance of two jet diameters $H = 2D$ is considered. This investigation is done numerically using a wall-resolved large-eddy simulation. Two geometrical arrangements are studied. These correspond to a jet impinging on a flat plate and a jet impinging on a hemispherical concave plate with a relative curvature $D/d = 0.089$, where d is the concave plate diameter. A detailed comparison shows that both flow configurations are very similar in terms of flow dynamics and heat transfer behaviors. The same mechanisms, coming from the initial jet instability and driving the heat transfer at the wall, are found for both geometries. However, a reduction of the mean wall heat transfer is reported for the jet impinging on the concave surface when compared to the flat plate impingement. This reduction mainly comes from the alleviation of the secondary peak. The deterioration of wall heat transfer is shown to be caused by a reduction in the intensity of the intermittent cold fluid injections generated by the secondary structures. These weaker events are assumed to be the consequence of the stabilizing normal pressure gradient, in the outer layer of the wall jet, induced by the concave curvature of the plate. This result goes against the current consensus, inherited from boundary layer studies, that is to say, that concave curvature enhances the heat transfer rate at the wall due to the formation of Görtler vortices. In an attempt to explain the contradictory result of the present study, a discussion is proposed in this paper showing that the commonly used analogy with boundary layer results must be made with care owing to several inherent differences between impinging jet and boundary layer flows.

DOI: 10.1103/PhysRevFluids.2.114608

I. INTRODUCTION

A submerged impinging jet is a fluid mechanics problem encountered in various fields ranging from meteorology, with the study of downbursts [1], to food processing [2] and cooling systems [3]. Such a technique has been widely used for cooling applications since it provides very high heat transfer rates highly localized in space. More specifically, in the aeronautical context, economical and environmental constraints have led engine manufacturers to work on the enhancement of thermodynamic engine efficiency. With current technologies, this is achieved by increasing the turbine entry temperature, which makes the cooling of high-pressure (HP) turbines mandatory to control the lifetime of the blades [3]. Today, jet impingement is one of the most common techniques used by the designers to cool the HP vanes. Therefore, many researchers have shown renewed interest in studying impinging jet flows, as can be seen from the numerous literature reviews on the subject [4–6]. Early studies were dedicated to correlations building [7] between several bulk parameters, e.g., jet diameter D, Reynolds number, and the average heat transfer rate at the wall, especially at the stagnation point. Such correlations are of major interest for engine manufacturers for the preliminary design phase. However, they are less suitable when one wants to achieve an

*pierre.aillaud@cerfacs.fr

optimal design as they do not reflect the detailed mechanisms involved in the heat transfer process, which may differ from one configuration to another. This certainly explains why the community has tried to understand the physical mechanisms affecting the wall heat transfer since the early detailed flow visualizations published by Popiel and Trass [8], highlighting the interaction between the well known vortical structures developing in a free jet and the impinged wall. A large number of studies focusing on the link between this unsteadiness present in impinging jet flows and the wall heat transfer can be found in the literature [9–17]. These basic studies, however, have mainly focused on the flat plate impingement.

Among the various parameters that may affect the heat transfer, e.g., group effect [10], the surface curvature is of particular interest as the jets near the leading edge impinge on a concave surface. This is a very specific application and studies on curved surfaces are not encountered as frequently as those on flat plates [18]. With curved surfaces a new geometrical parameter is introduced that is the relative surface curvature expressed as the ratio of the jet diameter to the concave plate diameter D/d. In the literature, two academic cases are usually studied: the impingement on a hemispherical plate and on a semicylindrical plate. For the first one, the flow is still axisymmetric as for most of the flat plate studies, while for the latter the axisymmetry is broken. The most studied configuration is the semicylindrical plate as it is similar to impingement near the leading edge for turbine blade cooling. It is often studied with multiple impinging jet arrangements adding complexity and making it difficult to isolate the effect of curvature on the heat transfer. As for the flat plate, some studies, for example, the work of Metzger *et al.* [19], have proposed empirical correlations between heat transfer at the wall and bulk parameters of interest for industrial designers. Other works have tried to relate the specific known dynamics of flow over a concave surface to heat transfer mainly based on the legacy from boundary layer flows. Gau and Chung [20] were interested in the evolution of the wall heat transfer for different Reynolds numbers, relative surface curvatures, and nozzle to plate distances for a two-dimensional convergent slot jet impinging on a semicircular concave surface. Their main observation was that at a fixed Reynolds number $\mathrm{Re} = 11\,000$, increasing the relative surface curvature enhances the local heat transfer distribution mainly outside the stagnation region. They attributed this positive effect on heat transfer to the generation of Görtler vortices resulting from a centrifugal instability along the concave walls. Note that there was no proof of the existence of these Görtler structures in their study and they only made a connection with previous studies for boundary layer flow on a concave wall [21]. One can also note that the results were compared quantitatively in terms of heat transfer, but the flow field was not characterized. Cornaro *et al.* [22] reported flow visualizations for a round impinging jet on a semicylindrical concave surface. They highlighted a strong interaction between a recirculating flow exiting the surface and the primary flow coming from the jet. The recirculating flow was shown to be entrained in the primary jet and the likelihood that stable ring vortices are formed in the shear layer was reduced. Therefore, it appears that the vortical structures developing in the free jet region, due to the initial Kelvin-Helmholtz instability, are affected by the relative curvature. As the relative curvature increases, the flow becomes less stable, the vortices break down as soon as they reach the plate, and the transition to turbulence is accelerated [22]. Note that they did not report heat transfer data. Later, Fenot *et al.* [23] performed an experimental study for a single round jet and multiple in-line round jets impinging on a semicircular concave surface for different jet to jet spacing. They compared their results obtained previously with the same experimental apparatus for an impinging jet on a flat plate. The concave plate was found to reduce the intensity of the local minimum and maximum in the heat transfer distribution. Comparisons with the flat plate with and without confinement shed light on the natural confinement generated by the curvature that possibly participates in the reduction of the wall heat transfer rates. They also tested different relative curvatures to highlight the effect on the heat transfer. Their results show that increasing the curvature has a limited impact on the heat transfer. Around the stagnation region, increasing the curvature slightly enhances the heat transfer rates, while for the greater curvilinear abscissa the opposite is observed. They proposed an explanation based on a combination of a confinement effect, reducing the wall heat transfer, and a curvature effect enhancing the wall heat transfer. Lee *et al.* [24] investigated the impingement on a hemispherical concave surface. Reported

results showed that curvature increases heat transfer rates, but only for the lowest Reynolds numbers investigated. On the reported curves at Re = 50 000, increasing the curvature does not impact the wall heat transfer. It should be noted that, except for Cornaro *et al.* [22], all the above-mentioned studies focused on heat transfer results and did not report any information about the flow field.

Based on this survey, it appears that the effect of concave curvature on heat transfer is not clear for impinging jet flows. Some studies report enhanced heat transfer attributed to Görtler vortices, without proof or visualization, while others show that the concave curvature has a detrimental effect. Moreover, the lack of a joint description of the flow dynamics and heat transfer adds to the uncertainty concerning the curvature effect. In addition to the experiments, Large Eddy Simulation (LES), giving access to the full three-dimensional (3D) instantaneous field, appears as a good candidate to study and understand the underlying physics involved for concave plates as well as to show how curvature affects the wall heat transfer. Assessment of the predictive capability of LES has already been done in the existing literature for impinging jet flows on flat plates with numerous studies that have provided important information to the understanding of such a flow [12,16,25–27]. The only publication reporting LES results for a jet impinging on a concave surface is by Jefferson-Loveday and Tucker [28]. This study is mainly focused on the comparison between a hybrid Reynolds-averaged-Navier-Stokes (RANS)-LES method or zonal approach and a wall-resolved LES. Moreover, they chose a relatively high nozzle-to-plate spacing $H = 6D$, where D is the jet diameter, compared to what is found in industrial applications in the context of turbine blade cooling ($H/D \approx 1$–2).

In an attempt to gain deeper insights into impinging jet flows over concave surfaces, the present study aims at analyzing the effect of surface curvature on the heat transfer using LES. This is achieved by comparing, for the same operating point, a jet impinging on a flat plate studied previously [16] and on a concave plate with a relative curvature $D/d = 0.089$, where d is the plate diameter. The concave flow configuration corresponds to the experimental setup of Lee *et al.* [24], which is a hemispherical plate. This choice is mainly motivated by the fact that the axisymmetry of the flow is preserved for this geometry, allowing to isolate the curvature effect.

The paper begins with the description of both flat and concave flow configurations in Sec. II. Then the numerical methods are described in Sec. III. A modification of the nozzle used for the previous flat plate simulation was necessary for the concave plate. The uncertainty related to such a change is assessed for the flat plate results in Sec. IV. Then uncertainty related to the grid resolution is investigated and the results are compared to the available experimental data in Sec. V. Detailed comparisons between the concave case and the flat plate case are provided in Sec. VI. Finally, the results are discussed in Sec. VII.

II. FLOW CONFIGURATION

The reference case used in this study to analyze the curvature effect is presented in Fig. 1. It is an axisymmetric unconfined three-dimensional submerged air jet impinging on a flat plate. The subsonic jet is isothermal with a temperature equal to the ambient temperature and impinges on a hot flat plate. The nozzle to plate distance H is 2 times the diameter of the jet D and the Reynolds number based on the bulk velocity U_b and D is $\mathrm{Re} = U_b D/\nu = 23\,000$, where ν is the kinematic viscosity of the fluid. The Mach number is $\mathrm{Ma} = U_b/c = 0.1$, where c is the sound speed and the fluid used is air with a Prandtl number $\mathrm{Pr} = 0.71$. The computational domain extends to $r/D = 3.5$ in the radial direction, where $r = \sqrt{x^2 + z^2}$ is the radial distance to the stagnation point defined as the intersection between the central axis of the jet and the plate. This configuration has been widely studied in the literature [12,29,30]. The results obtained for this reference case and the validation of the LES are not detailed in this paper, but the reader is referred to previously published works for more information [16,25].

The concave plate configuration consists of a single axisymmetric submerged air jet, $\mathrm{Pr} = 0.71$, impinging on a hemispherical plate. This setup was studied experimentally by Lee *et al.* [24]. A three-dimensional representation of the geometry along with the coordinate system are shown in

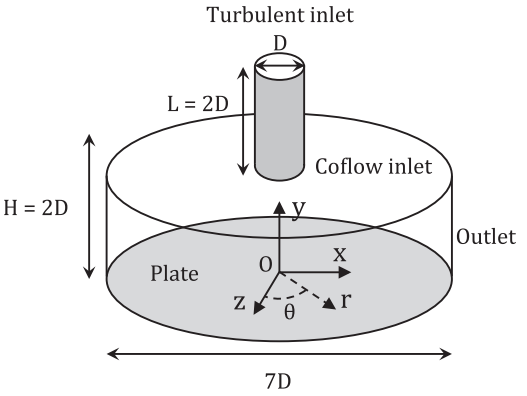

FIG. 1. Schematic view of the flat plate configuration with the associated coordinate system. The origin O is located on the plate at the nozzle geometrical center and the y axis is normal to the plate pointing inward; r is the radial distance to the origin and θ the azimuthal angle ($\theta = 0$ is placed along the x axis).

Fig. 2(a). The relative curvature is $D/d = 0.089$, where d is the concave plate diameter and the nozzle to plate distance is $H = 2D$. The latter is defined as the distance along the y axis between the nozzle outlet plane and the stagnation point on the plate at $s/D = 0$, where s is the curvilinear abscissa shown in Fig. 2(b). The plate extends from $s/D = 0$ at the stagnation point to $s/D = 8.8$

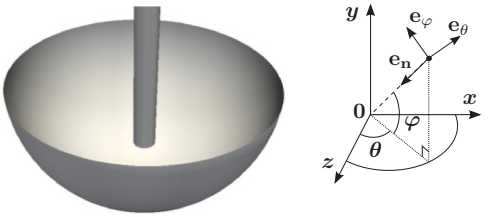

(a)

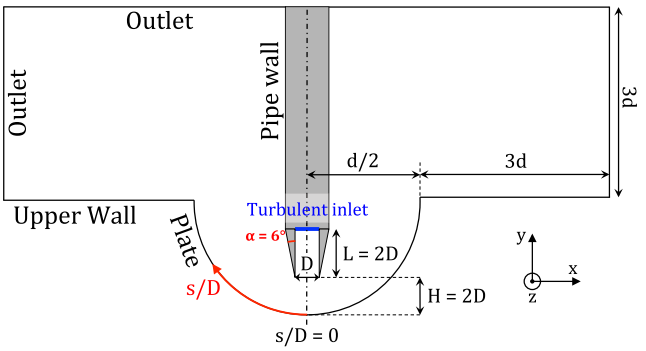

(b)

FIG. 2. (a) Three-dimensional representation of the concave geometry along with the spherical coordinate system. The origin is located at the center of the hemisphere; θ and φ are the azimuthal and polar angles, respectively; $\mathbf{e_n}$ is the axis normal to the plate pointing inward; $\mathbf{e}_\varphi$ is the axis in the polar direction; $\mathbf{e}_\theta$ is the axis oriented in the azimuthal direction. (b) Cut of the geometry through a plane tangent to the pipe axis.

at the end of the hemisphere. The Reynolds number based on U_b and D is $\mathrm{Re} = 23\,000$ and the jet is subsonic with a Mach number $\mathrm{Ma} = U_b/c = 0.15$. This operating point has been chosen for two reasons: It is representative of the operating conditions in a real engine and it is identical to the operating point of the flat plate case used for the comparisons [16]. One can note that the computational domain in Fig. 2(b) is large compared to the region of interest. Due to the concave curvature, a large axisymmetric toroidal vortex is formed because of the recirculating flow exiting the plate [22]. The computational domain is extended to avoid interactions between this large-scale vortex and the outlets. Similar issues were reported by Jefferson-Loveday and Tucker [28].

To keep the injection pipe of length $2D$, as in the flat plate case, it is necessary to use a beveled nozzle as shown in Fig. 2(b). The bevel angle is kept as small as possible to limit the impact on the flow in such a way that the jet and entrained ambient flows merge at an angle $\alpha = 6^\circ$. The impact of this modification on the flat plate results is discussed in Sec. IV.

Finally, one can note that the Richardson number $\mathrm{Ri} = g\beta(T_w - T_\infty)D/U_b^2$, with g the gravitational acceleration and β the thermal expansion of air, is of the order of 10^{-5} for both configurations, meaning that the buoyancy effects are negligible, i.e., the heat transfer is governed by forced convection.

III. NUMERICAL METHODS

This section is dedicated to the description of the numerical methods used to address the present problem. The solver is first described along with the inherent approximations, issued by the numerical schemes and the various turbulence closures and models. Then the treatment of boundary conditions is discussed.

A. Solver

The parallel LES solver AVBP [31] developed at CERFACS and IFP-EN is used to solve the 3D filtered compressible Navier-Stokes equations. A finite-element two-step time-explicit Taylor-Galerkin scheme (TTG4A) [32] is used for the discretization of the convective terms based on a cell-vertex formulation. The scheme provides fourth-order accuracy in time and third-order accuracy in space while ensuring low dispersion and diffusion properties, which is in agreement with the requirements of LES applications [33]. A second-order Galerkin scheme is used for the diffusion terms [34]. Such numerics are especially designed for LES on hybrid meshes and have been extensively validated in the context of turbulent flow applications [27,35–38]. The unresolved subgrid scale (SGS) stress tensor is modeled using the Boussinesq assumption [39] and the SGS viscosity μ_{SGS} is computed with the wall adapting local eddy-viscosity model (WALE) [40] that is well suited for wall-resolved LES as it recovers the proper y^3 near-wall scaling of the eddy viscosity [41] contrarily to the more conventional Smagorinsky model [42]. The SGS heat flux vector is modeled using the classical gradient-diffusion hypothesis [39] that relates the SGS heat flux to the filtered temperature gradient using a SGS thermal conductivity λ_{SGS}. This approach postulates a direct analogy between the momentum and heat transfer through the SGS turbulent Prandtl number $\mathrm{Pr}_{\mathrm{SGS}} = \mu_{\mathrm{SGS}} C_p/\lambda_{\mathrm{SGS}}$, here fixed at $\mathrm{Pr}_{\mathrm{SGS}} = 0.5$, where C_p is the specific-heat capacity at constant pressure.

B. Boundary conditions

This section is dedicated to the description of the boundary conditions for the concave configuration. The reader is referred to the work of Aillaud *et al.* [16] for more details about the flat plate case.

The treatment of the different boundaries identified in Fig. 2(b) is detailed hereinafter. A mean velocity profile is weakly imposed at the inlet of the pipe associated with a uniform temperature $T_\infty = 300$ K using the Navier-Stokes characteristic boundary condition (NSCBC) formalism [43]. Note that the jet temperature equals the ambient temperature. The experiment does not report any

measurements in terms of velocity profile at the nozzle exit. Therefore, the axial velocity, i.e., the velocity along the y direction, is prescribed using the classical empirical power-law profile for fully developed turbulent pipe flows [44] given in Eq. (1), while the other components are set to zero,

$$\frac{U(r)}{U_{\text{ce}}} = \left(1 - \frac{2r}{D}\right)^{1/7.23}, \tag{1}$$

where U_{ce} is the centerline velocity and $r = \sqrt{x^2 + z^2}$ represents the radial distance to the jet axis. It is known that, for turbulent pipe flows, the ratio of the bulk velocity to the centerline velocity U_b/U_{ce} depends on the Reynolds number [44]. Therefore, the exponent $1/7.23$ is determined from Eq. (2) following the expression of Cooper *et al.* [45] to reach the correct ratio,

$$\frac{U_b}{U_{\text{ce}}} = 0.811 + 0.038[\log_{10}(\text{Re}) - 4]. \tag{2}$$

To mimic the turbulent flow developing in the nozzle, isotropic velocity fluctuations are injected at the inlet using a Passot-Pouquet spectrum and following a nonreflecting formalism to avoid numerical noise [46]. The most energetic length scale that defines the peak in the spectrum is set to $D/3$ and the amplitude of the injected velocity fluctuations is set to $0.05U_b$. Note that the same setup is used at the inlet of the flat plate simulation.

At the outlets, the static pressure is relaxed towards a mean reference pressure $P_\infty = 101\,325$ Pa using the NSCBC formalism accounting for the transverse terms [47]. The nozzle walls are adiabatic with a no-slip condition imposed. The plate is treated as an isothermal no-slip wall with $T_w = 330$ K. As a hybrid strategy is chosen for the mesh generation, i.e., prisms at the wall and tetrahedral elements inside the domain, the upper wall is necessary to avoid the generation of pyramidal elements due to the degeneration of the prism layers. This upper wall (see Fig. 2) is treated as an adiabatic slip wall. The use of a slip condition is mainly motivated by its ability to model the air entrainment present in the experiments where such a wall is not present. Moreover, it is unlikely that this boundary condition affects the results as it is located relatively far from the region of interest.

IV. IMPACT OF THE BEVELED NOZZLE FOR THE FLAT PLATE

Jet flows are known to be sensitive to injection conditions. A large domain, shown in Fig. 2, has to be used for the concave setup and the injection pipe is immersed in the computational domain. Hence, a beveled nozzle is used to keep the injection pipe of length $2D$ present for the flat plate LES. However, this beveled nozzle is different from the one used for the flat plate configuration. Therefore, this section intends to show that the alteration of the nozzle does not modify significantly the heat transfer results for the reference flat case.

A new configuration with a beveled injection, referred to as injection 2, is simulated using LES for the flat plate case. The same numerical setup and the same spatial resolution as described by Aillaud *et al.* [16] are used. Inlet, outlet, and plate boundary conditions are treated in the same way as described in Sec. III B. The geometry used for the LES with injection 2 is shown in Fig. 3. The results are compared to the original geometry, referred to as injection 1, presented in Fig. 1. An overview of major modifications can be evidenced by looking at the wall heat transfer results. Indeed, for an impinging jet similar to the one studied here, the heat transfer results are known to be sensitive to the mean flow and the jet dynamics [5,18]. Hence, only the heat transfer results are compared in terms of Nusselt number defined as

$$\text{Nu}(r) = q_w(s)D/(\lambda_f(T_w - T_\infty)), \tag{3}$$

where $q_w(s)$ is the temporally and azimuthally averaged wall heat flux and λ_f is the thermal conductivity of air at T_w. Due to strong similarities in terms of mean flow field and jet dynamics between injections 1 and 2, good agreement is found for the radial evolution of the Nusselt number in Fig. 4. In addition, a thorough comparison, not shown here, shows no alteration of the mean flow field and the jet dynamics.

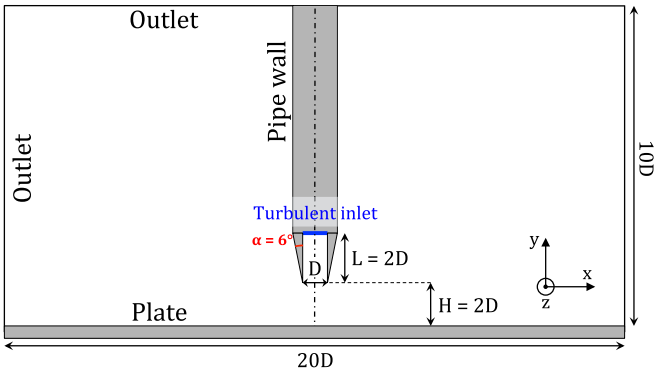

FIG. 3. Schematic view of the beveled injection, referred to as injection 2, used for the new flat plate LES.

The use of the beveled nozzle is therefore not the primary parameter affecting the jet behavior and the heat transfer at the wall for the present study. Hence, injection 1 used for the reference flat plate case (see Fig. 1) by Aillaud *et al.* [16] can be used for the comparisons to study the effect of the concave curvature on the flow dynamics and the wall heat transfer.

V. VALIDATION FOR THE CONCAVE PLATE: COMPARISONS WITH THE AVAILABLE EXPERIMENTAL DATA AND EVALUATION OF NUMERICAL UNCERTAINTIES

In addition to the classical LES problem of defining boundary conditions that match an experimental facility, assuming that all information is known [48,49], LES is subject to several uncertainties. For instance, grid resolution is one degree of freedom that can have a strong influence on the numerical predictions. As part of the validation process, two spatial resolutions, whose properties are presented in Sec. V A, are used to assess the uncertainty linked to the grid in Sec. V B. Whenever possible, the results are compared to the available experimental data published in the literature.

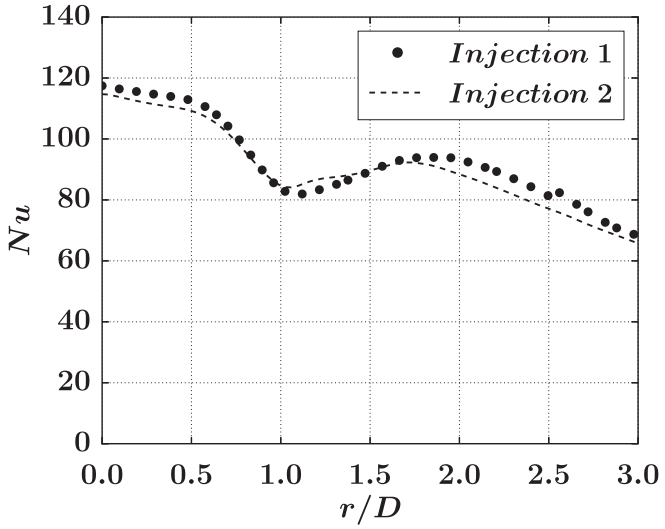

FIG. 4. Nusselt number Nu as a function of the distance to the stagnation point r/D for the flat plate for the original, i.e., injection 1 (Fig. 1), and the beveled, i.e., injection 2 (Fig. 3), nozzles: •, injection 1; ——, injection 2.

TABLE I. Computational grid properties for the two different spatial resolutions $M1$ and $M2$.

Property	$M1$	$M2$
number of grid cells (millions)	94	124
number of prisms (% of the total number of cells)	21%	25%
free jet region ($\Delta l/D$)	2.0×10^{-2}	2.0×10^{-2}
prism height ($\Delta n/D$)	2.1×10^{-3}	1.3×10^{-3}
minimum number of points in the inner layer of the wall jet	5	10
n^+	1.5–4	1–2.5
$r^+ \approx r\theta^+$	7.5–20	5–12.5
dt (μs)	0.12	0.06
CPU time for 1 cycle (hours)	1300	3900
OCCIGEN BULL cluster (CINES)		

In Secs. V and VI, the total physical time used to construct the statistics represents about 20 cycles, if not specified otherwise, where the cycle period is evaluated from the frequency f corresponding to the impinging frequency of the main large-scale structures in the simulation ($\mathrm{St}_D = fD/U_b \approx 0.78$ based on pressure and wall heat flux signal analysis). The temporal averaging procedure starts when the flow becomes statistically stationary. Note also that to increase the convergence of the statistics, quantities of interest are averaged in the homogeneous azimuthal direction, whenever possible, after temporal averaging.

A. Grids properties

One of the main source of uncertainty in LES is linked to the grid resolution and *a priori* meshing criteria for impinging jet flows are not currently available. Three important regions known as the free jet, the wall jet, and the near wall require particular attention for the grid generation. The unique explicit mesh criterion is given by the wall-resolved target. This requires one to put the first off-wall point inside the viscous sublayer at $n^+ = u_\tau n/\nu < 3$–5, where u_τ is the friction velocity and n is the normal distance between the wall and the first off-wall point. A hybrid meshing strategy is chosen for this study with tetrahedral elements inside the volume and ten prism layers at the wall. All prisms have the same height. The aspect ratio, defined as the ratio of the surface triangle characteristic edge length Δl to the prism height, is set to 5. As a starting point for the mesh generation, the grid resolution is kept identical to the finest mesh used for the validated LES of the reference flat plate case [16]. As this study compares two impinging jet simulations, this choice prevents an alteration of the initial instability of the jet caused by a modification of the spatial resolution. Moreover, this grid resolution was found to produce predictions in agreement with the available experimental results for the well documented flat plate setup. In the following, this first mesh is referred to as $M1$. *A posteriori* evaluation shows that there are five points in the inner layer of the wall jet for $s/D < 0.5$. This region corresponds to the finest inner layer thickness of the wall jet that is nearly constant as for steady stagnation plane flows [44]. Further downstream, the wall jet thickens and there are approximately ten points in the inner layer at $s/D = 1.0$.

The mesh $M1$ was originally designed for the flat plate, but the concave plate introduces additional mechanisms near the wall linked to inertial forces. Therefore, to ensure that the physics induced by the curvature is not altered by the grid resolution, a second mesh, referred to as $M2$, is generated. The spatial resolution in the free jet region remains unchanged to avoid modifications of the initial instability of the jet from grid resolution changes. However, at the wall a finer spatial resolution is used. The height of the first prism layer is reduced, leading to approximately ten points in the inner layer of the wall jet for $s/D < 0.5$ and 15 points at $s/D = 1$. The grid properties are summarized in Table I. The normalized wall distance n^+ values for the first off-wall points are presented in Fig. 5 for the two grid resolutions. For both grids, the first off-wall points are located inside the viscous

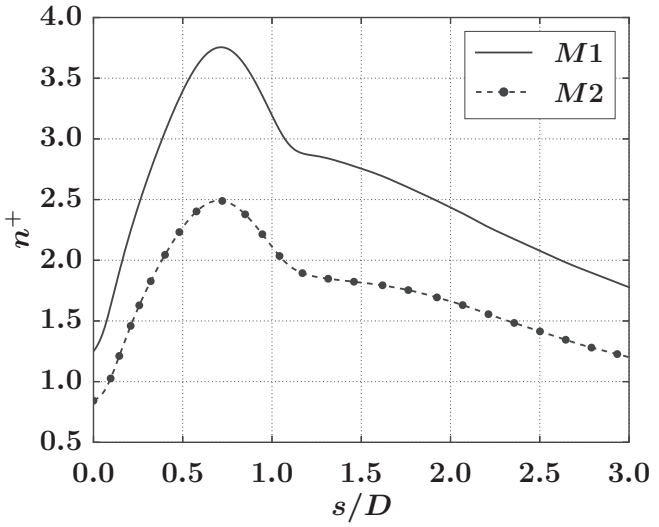

FIG. 5. Normalized wall distance n^+ on the plate as a function of the curvilinear distance to the jet axis s/D for grids −, $M1$; - -●- -, $M2$. See Table I for grids properties.

sublayer, i.e., $n^+ < 5$. For $M2$ the prism height is reduced, leading to a decrease of the normalized wall distance n^+. For these spatial resolutions, the ratio of the n^+ values is similar to the ratio of the prisms height for $M1$ and $M2$, meaning that the first off-wall points are indeed located inside the viscous sublayer, i.e., in the linear region.

B. Validation and numerical uncertainties

The results obtained with both grids $M1$ and $M2$ are presented in Sec. V B. As the resolution is modified only in the near-wall region, the comparison between both meshes focuses on the wall jet and the wall quantities in Secs. V B 1 and V B 2, respectively. Comparisons with the experimental data of Lee *et al.* [24] are provided for the wall quantities in Sec. V B 2.

1. Wall jet

Lee *et al.* [24] did not report a characterization of the flow field and there is no other study dealing with this configuration. Hence, the only possibility for the wall jet is to do a relative comparison between the two meshes. The mean wall jet is compared for both grids in Fig. 6 showing the mean polar velocity profiles at different curvilinear abscissas. The polar velocity is defined as $U_\varphi = \mathbf{U} \cdot \mathbf{e}_\varphi$, where $\mathbf{U}$ is the velocity vector in the Cartesian coordinate system and $\mathbf{e}_\varphi$ is defined in Fig. 2(a). The refinement in the near-wall region for $M2$ does not impact significantly the development of the mean wall jet. The maximum polar velocity is similar and located at the same normal distance from the wall for both grids. The mean normal velocity profiles at $s/D = 0.5$ and 1.0 are presented in Fig. 7. The normal velocity is defined as $U_n = \mathbf{U} \cdot \mathbf{e_n}$, where $\mathbf{e_n}$ is the normal unit vector defined in Fig. 2(a). The mean normal velocity shows very little sensitivity to the grid resolution. The biggest differences appear at $s/D = 1.0$, where the magnitude of the normal velocity is of the order of a few percent of the bulk velocity.

The root-mean square (rms) of the velocity fluctuations at $s/D = 0.5$ and $s/D = 1.0$ is also presented in Figs. 8 and 9. The shapes of the profiles are similar for both meshes and the use of a finer spatial resolution impacts mainly the levels of these fluctuations. The biggest difference is observed for U_n' at $s/D = 1.0$ in Fig. 9. The peak amplitude predicted by $M2$ is 3% lower than the $M1$ result.

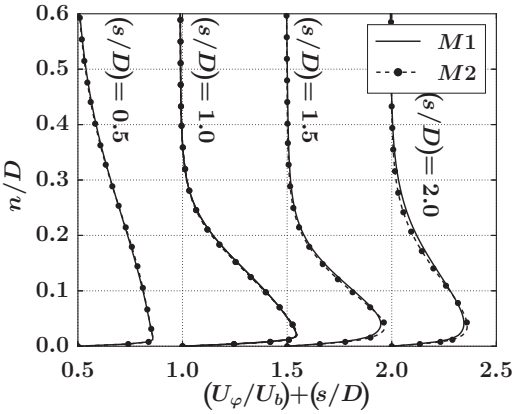

FIG. 6. Mean polar velocity U_φ/U_b as a function of the normal distance to the wall n/D at the curvilinear positions $s/D = 0.5$, 1.0, 1.5, and 2.0: −, $M1$; - -●- -, $M2$. See Table I for grids properties.

2. *Wall quantities*

In terms of wall quantities, Lee *et al.* [24] provided the wall pressure coefficient distribution defined in Eq. (4),

$$C_p = \frac{P_w(s) - P_\infty}{0.5\rho_\infty U_{\text{ce}}^2}, \tag{4}$$

where $P_w(s)$ is the local static pressure on the concave plate, P_∞ is the ambient pressure, ρ_∞ is the fluid density at ambient conditions, and U_{ce} is the mean centerline velocity at the nozzle exit. They have also provided the Nusselt number distribution along the curvilinear abscissa.

Comparisons for the mean wall pressure coefficient are shown in Fig. 10. The total pressure is conserved between the nozzle exit and the plate and since the compressibility effects are limited (Ma = 0.15), the wall pressure coefficient equals one at the stagnation point. The length of the stagnation region linked to the favorable pressure gradient in the positive s/D direction is well recovered by both $M1$ and $M2$. The intensity of the favorable pressure gradient, given by the slope of C_p, is also in agreement with the experimental results for both grids.

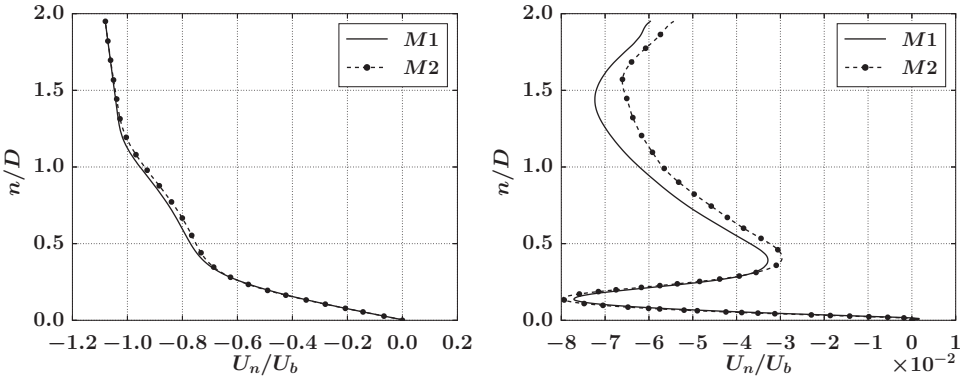

FIG. 7. Mean normal velocity U_n/U_b as a function of the normal distance to the wall n/D at the curvilinear positions (a) $s/D = 0.5$ and (b) $s/D = 1.0$: −, $M1$; - -●- -, $M2$. See Table I for grids properties.

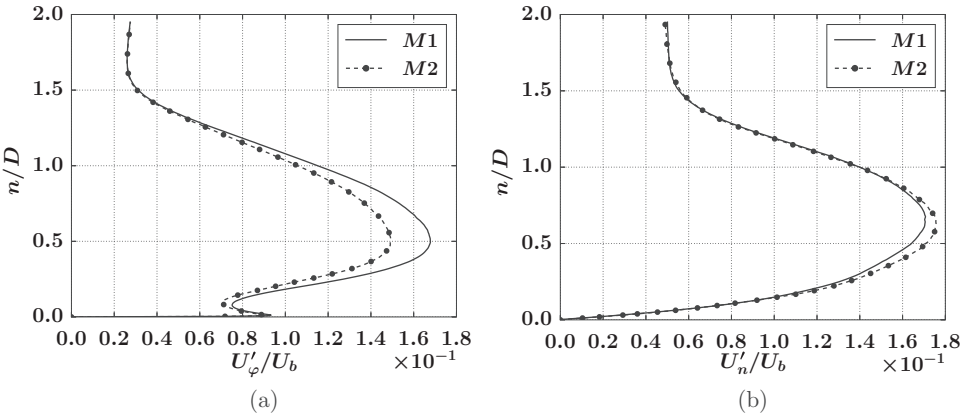

FIG. 8. Root mean square of the (a) polar velocity fluctuations U'_φ/U_b and (b) normal velocity fluctuations U'_n/U_b as a function of the normal distance to the wall n/D at the radial position $s/D = 0.5$: —, $M1$; - -●- -, $M2$. See Table I for grids properties.

Finally, the Nusselt number distribution is shown in Fig. 11. First, one can note a relatively small dependence of the Nusselt number on the grid resolution used for this study. The noticeable difference is located at the stagnation point where for $M2$ the Nusselt number is slightly lower than for $M1$. This leads to a relative difference of 5% if $M2$ is taken as the reference. However, for both meshes, the Nusselt number distribution does not exhibit a significant secondary peak as reported in the experiment. Rather, a plateau is seen similarly to previously reported experimental results of such a problem but for a cylindrical plate [23]. One can note that $M2$ exhibits a slight inflection of the Nusselt number curve at $s/D \approx 1.25$, but the slope remains relatively small. When LES is compared to the experimental results, discrepancies also appear in the stagnation region. The heat transfer in this stagnation region is mainly driven by the mean flow field and turbulence from the pipe [5] that are not characterized in the experiment of Lee *et al.* [24] used here for the comparisons.

An accurate validation process for a simulation requires comprehensive experimental databases characterizing the flow dynamics as well as the heat transfer. This applies especially for impinging jet flows, when one wants to validate a simulation or compare experimental results, as it is known that

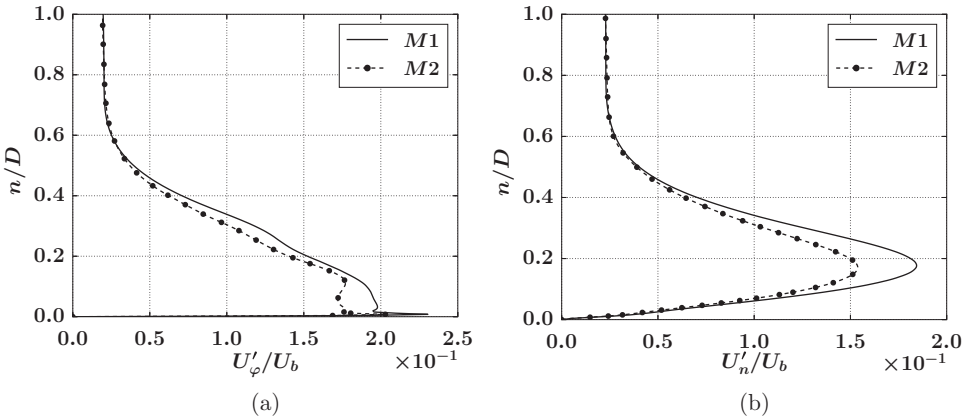

FIG. 9. Root mean square of the (a) polar velocity fluctuations U'_φ/U_b and (b) normal velocity fluctuations U'_n/U_b as a function of the normal distance to the wall n/D at the radial position $s/D = 1.0$: —, $M1$; - -●- -, $M2$. See Table I for grids properties.

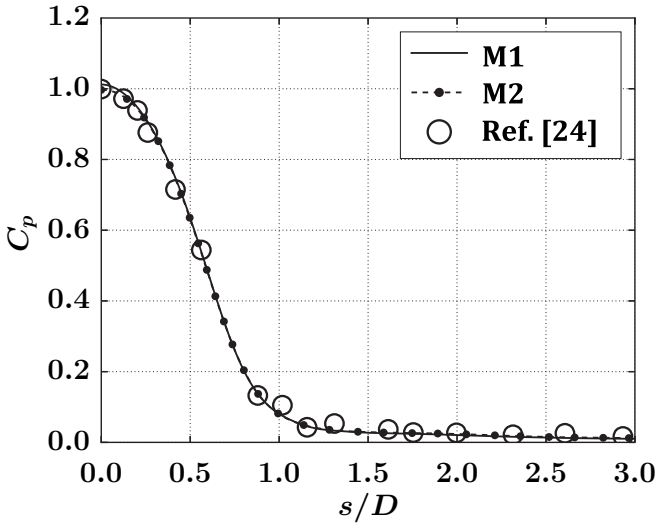

FIG. 10. Mean wall pressure coefficient C_p as a function of the curvilinear distance s/D: ◯, Ref. [24]; −, $M1$; - -●- -, $M2$. See Table I for grids properties.

the wall heat transfer is driven by the mean flow field, turbulence from the pipe, and jet unsteadiness [5,12,15,16,18]. Such experimental databases are not currently available for a jet impinging on curved plates.

Nevertheless, it was possible to assess the impact of the grid resolution that is a major source of uncertainty for LES. It was demonstrated that the grid resolution $M1$, coming from a validated LES for a jet impinging on a flat plate [16], is sufficient to consider that the statistics are converged in terms of spatial resolution. Discrepancies are observed between the current LES results and the available experimental results for the Nusselt number [24]. One can note that there is only one

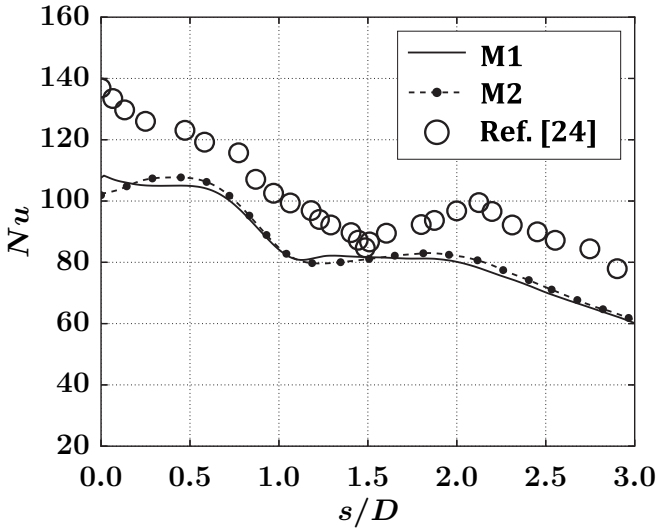

FIG. 11. Mean Nusselt number Nu as a function of the curvilinear distance s/D: ◯, Ref. [24]; −, $M1$; - -●- -, $M2$. See Table I for grids properties.

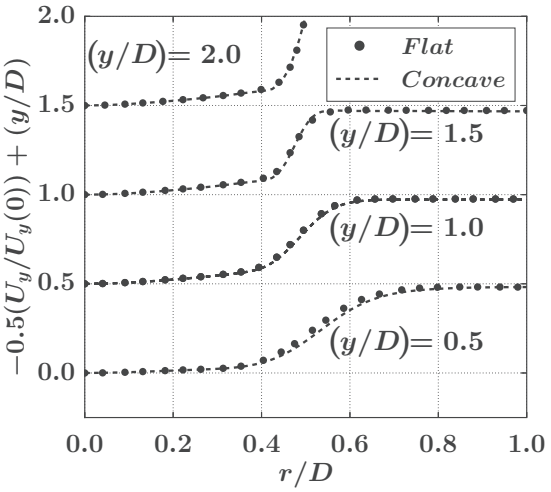

FIG. 12. Mean y component of the velocity vector $U_y/U_y(0)$, where $U_y(0)$ is the velocity on the jet axis, as a function of the axial position y/D. The profiles are located from top to bottom at $y/D = 2.0$, 1.5, 1.0, and 0.5: •, flat plate; −−, concave plate.

experimental study [24] in the literature dealing with this flow configuration. It is rather limited considering the variability of the results found in the published data for the flat plate at similar operating conditions [5]. Therefore, without information about the dynamics of the jet studied experimentally, discrepancies with the available experimental data, in terms of Nusselt number, are thought to be acceptable. In addition, it is worth recalling that the main objective here is a comparison with the flat plate simulation [16] using the same method, the same grid resolution, for which all information is known and a deeper validation was possible.

Knowing that this unsteady LES database can be confidently used to characterize the surface curvature effect on the heat transfer at the wall. For all the following, the LES prediction obtained with $M1$ is used as it has been shown that this spatial resolution is adequate to consider grid convergence.

VI. CHARACTERIZATION OF THE CURVATURE EFFECT

In an attempt to characterize the curvature effect, this section presents a detailed comparison between the jet impinging on the flat plate and on the concave plate. It is organized as follows. First the main statistics in the free jet and wall jet are analyzed in Sec. VI A. Next the flow organization is described and compared for both cases in Sec. VI B. Then a link is established between the highlighted flow features and the heat transfer at the wall in Sec. VI C. Finally, the wall heat transfer is characterized in terms of statistical behavior by looking at probability density functions and low-order as well as high-order statistics such as the skewness in Sec. VI D.

A. Main statistics

The mean development of the free jet is presented for both the flat and concave cases in Fig. 12, showing the profiles of the mean axial velocity U_y at different axial locations. These profiles show that the mean free jet behaves similarly for both configurations. For the concave case, the shear layer thickens in the same way as for the flat plate. It seems, therefore, that the mean free jet is not disturbed by the recirculating flow coming from the wall jet exiting the plate. The fluctuating component of the flow is presented in Fig. 13, showing the rms of the axial velocity fluctuations. There is no significant alteration of the fluctuating field due to the concave curvature. These comparisons highlight that the

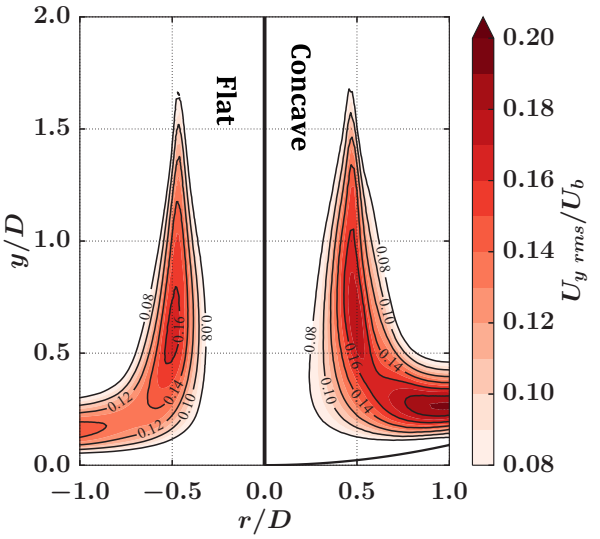

FIG. 13. Filled contours of the rms of the axial velocity fluctuations $U_{y\,\mathrm{rms}}/U_b$ in the $(y/D,r/D)$ plane. Negative r/D values correspond to the flat plate geometry, while positive r/D values correspond to the concave plate.

concave curvature does not modify significantly the first- and second-order statistics in the free jet region.

When approaching the plate, the flow is deflected and a wall jet develops along the plate. The wall jet development is compared qualitatively for both cases in Fig. 14(a). For this comparison, the concave plate is flattened. Note that for the flat plate, r/D is replaced by s/D as it represents the same information, i.e., the distance from the jet axis along the wall. In the flattened frame, the polar velocity U_φ is equivalent to the radial velocity U_r used for the flat plate. Qualitatively, the wall jet develops similarly for both flat and concave plates with first an acceleration due to the presence of the stagnation region where a favorable streamwise pressure gradient exists. The maximal radial velocity

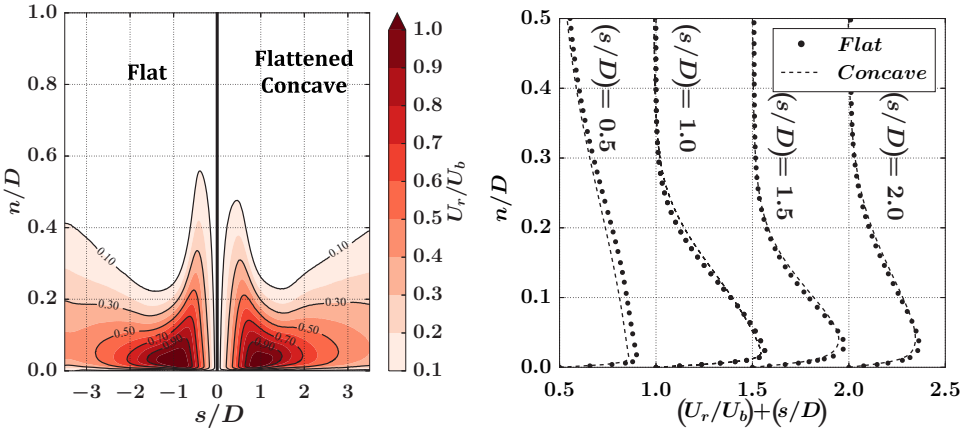

FIG. 14. (a) Mean radial velocity U_r/U_b in the $(n/D,s/D)$ plane. Negative s/D values correspond to the flat plate geometry, while positive s/D values correspond to the flattened concave plate. (b) Mean radial velocity profile extracted at $s/D = 0.5$, 1.0, 1.5, and 2.0 (b): •, flat plate; −−, concave plate.

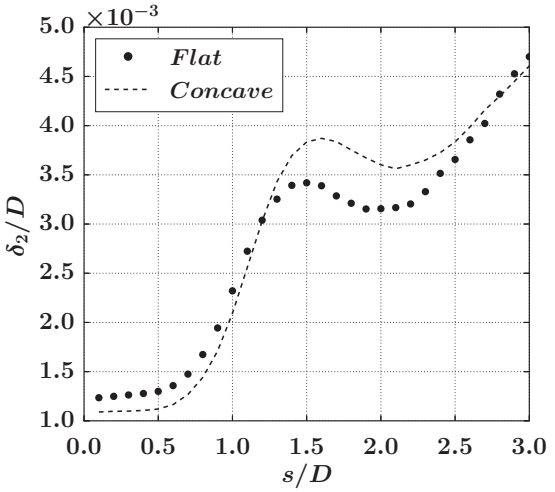

FIG. 15. Momentum thickness δ_2/D, defined in Eq. (5), as a function of the distance from the jet axis s/D: •, flat plate; −−, concave plate.

in the wall jet is reached at $s/D \approx 1$ and is of the order of U_b. Then, due to the radial expansion and the mass conservation, the wall jet decelerates. This deceleration is located at a similar radial position for both cases. The mean radial velocity profiles, shown in Fig. 14(b), confirm again that the mean flow field is not significantly impacted by the concave curvature of the plate.

To go further in the characterization of the wall jet, the development of the inner layer is compared for both flat and concave plates. The inner layer is defined as the layer going from the wall to the maximum velocity. Its development can be characterized by looking at integral quantities, such as the momentum thickness, whose definition is adapted to the wall jet flow in Eq. (5),

$$\delta_2(s) = \int_0^{n_{\max}(s)} \frac{U_r(n)}{U_{\max}(s)}\left(1 - \frac{U_r(n)}{U_{\max}(s)}\right)dn, \tag{5}$$

where $U_{\max}$ is the maximum velocity in the wall jet, at the considered position s/D, and $n_{\max}$ is the location of $U_{\max}$ in the direction normal to the plate. The evolution of the momentum thickness δ_2/D along the plate is presented in Fig. 15. Again, the development on the concave plate is analogous to the development of the wall jet for the flat plate. For $s/D < 0.5$, the inner layer starts to evolve under the influence of the impinging flow and the momentum thickness is quasiconstant. Then the wall jet thickens with nearly the same slope for both plates. At $s/D \approx 1.5$, the development is perturbed by the interaction with the coherent structures initiated in the shear layer of the free jet [8] and discussed in Sec. VI B 1. This interaction induces the transition to a fully turbulent wall jet that continues its development with a momentum thickness increasing linearly.

B. Large-scale organization

1. Instantaneous visualizations

The classical description of the instantaneous large-scale organization for impinging jet flows, at Reynolds number close to the present study, involves an initial Kelvin-Helmholtz instability followed by a roll-up of the shear layer into vortical structures with a strong azimuthal coherence [8]. These structures are commonly referred to as primary structures. Secondary structures originate from the unsteady boundary layer separation caused by the unsteady adverse pressure gradient coming from the interaction between the primary structures and the wall [50]. Another important coherent structure developing in a jet is a streamwise-oriented vortex emerging between the primary structures [51–55] due to azimuthal instabilities and vortex stretching [56] (see Fig. 16). These longitudinal vortices

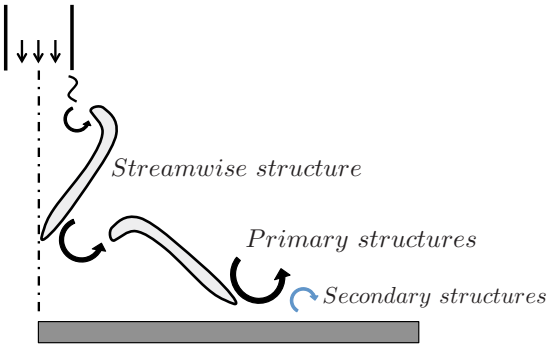

FIG. 16. Illustration of the streamwise-oriented structures originating in the shear layer of the free jet region in impinging jet flows.

were called ribs by Hussain [56] and have also been observed for a plane shear layer [57]. Unlike the primary and secondary vortices, they are not coherent in the azimuthal direction but exhibit a spatial periodicity. These streamwise structures play an important role in the transition process of a free jet as they increase the three dimensionality of the flow. Their principal characteristic, which makes them easy to distinguish, is that they are tilted as shown in Fig. 16. These structures are often overlooked in the existing literature about impinging jets for which the focus is more on the azimuthally coherent vortices.

A 3D visualization of the different coherent structures is proposed for the free jet and the wall jet regions in Figs. 17 and 18, respectively. The rotational structures are visualized using a positive isosurface of the Q criterion [58] that compares the Euclidean norm of the antisymmetric part of the velocity gradient tensor, i.e., the rate-of-rotation tensor, to the Euclidean norm of the symmetric part of the velocity gradient tensor, i.e., the rate-of-strain tensor. First, the primary structures are identified in Fig. 17 in the form of azimuthally coherent isosurfaces. One can note that in both cases, the primary structure is subject to an azimuthal distortion as shown by the wavy isosurfaces. This instability has been studied previously for vortex ring by Widnall and Sullivan [59] and the number of waves has been shown to depend on, among others, the Reynolds number [60]. It is this specific

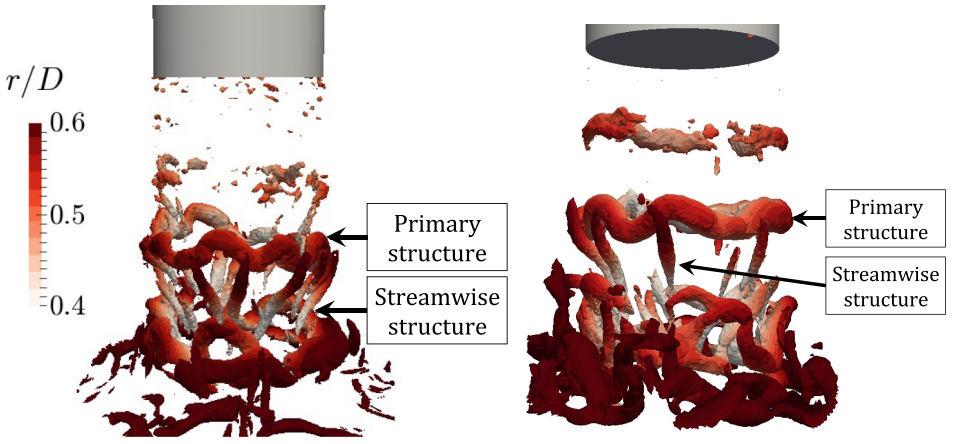

FIG. 17. Isosurface of the Q criterion $Q = 28U_b^2/D^2$ in the free jet region, colored by the radial distance to the jet axis r/D for (a) the flat plate and (b) the concave plate.

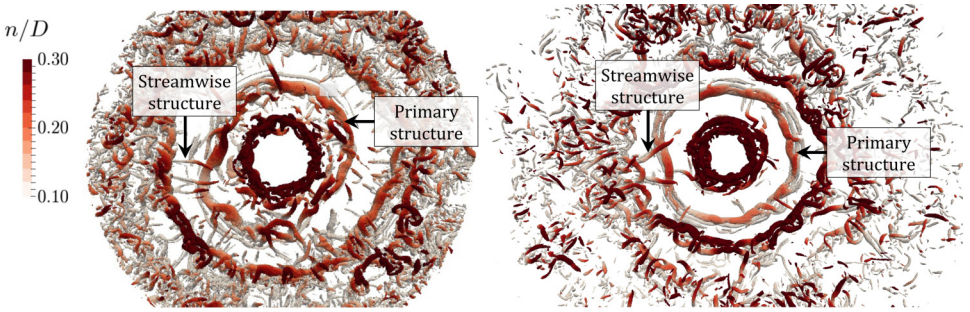

FIG. 18. Top view of the isosurface of the Q criterion $Q = 28U_b^2/D^2$ in the wall jet region, colored by the normal distance to the wall n/D for (a) the flat plate and (b) the concave plate.

azimuthal instability that generates the streamwise vortices [61] that can be observed between the primary structures in Fig. 17. They are recognizable by their characteristic tilt towards the jet core. Note that the number of streamwise vortices depends also on the Reynolds number. After being convected by the free jet flow, these structures impinge on the wall and are deflected in the radial direction. Most of the time, they are able to resist the impingement process and they are found again in the wall jet region as shown in Fig. 18. Again, the primary and streamwise structures are clearly seen for both flat and concave plates.

These flow visualizations give insight into the instantaneous organization of the flow field that seems *a priori* similar for both configurations. To go further in the characterization of the unsteadiness present in both jets, a modal analysis is proposed in Sec. VI B 2.

2. *Modal analysis*

Based on the previous instantaneous visualizations, the spectral content of the two flow configurations is investigated. Taking advantage of the spatial and temporal information provided by the LES, the dynamic mode decomposition (DMD) [62] is used to get additional knowledge about the flow organization. The fundamental idea of DMD is to assume that a linear relation exists between successive snapshots throughout the sampling period. Dynamic mode decomposition, working with time-evolving spatial fields, is chosen because it enforces orthogonality in time giving spatial structures that are single frequential as desired here. Compared to the classical Fast Fourier transform (FFT) where the frequencies are known *a priori*, based on the frequency resolution, the DMD frequencies are obtained through a least-squares fit to the data. The DMD has the following advantages compared to the FFT: less spectral leakage, works with short signals, and takes advantage of the large amount of spatial information.

To perform the DMD analysis, $2D$ cuts are considered in the $(y/D,r/D)$ plane. The whole snapshot sequence represents approximately ten cycles where one cycle is based on $\mathrm{St}_D = 0.78$. The sampling rate is chosen to have approximately 15 snapshots per cycle for both flow configurations leading to a cutoff frequency of $\mathrm{St}_D = 6$. These analyses concern the azimuthally coherent structures, i.e., primary and secondary vortices. The DMD is performed on the pressure signal. Indeed, it is a good indicator of the presence of a coherent structure in this case due to the local pressure minimum caused by their rotational motion.

The identification of the dynamically important modes is based on the analysis of the amplitude spectra yield by the DMD and shown in Fig. 19. This spectrum represents the area-weighted average amplitude of each mode identified by the DMD algorithm. The DMD highlights the presence of two dominant modes. The first one, referred to as mode 1, is a high-frequency mode identified at $\mathrm{St}_D = 1.58$. It is probably related to the initial shear layer instability. The second one, referred to as mode 2, corresponds to $\mathrm{St}_D = 0.78$, which is half the frequency of mode 1. Mode 2 is likely to be

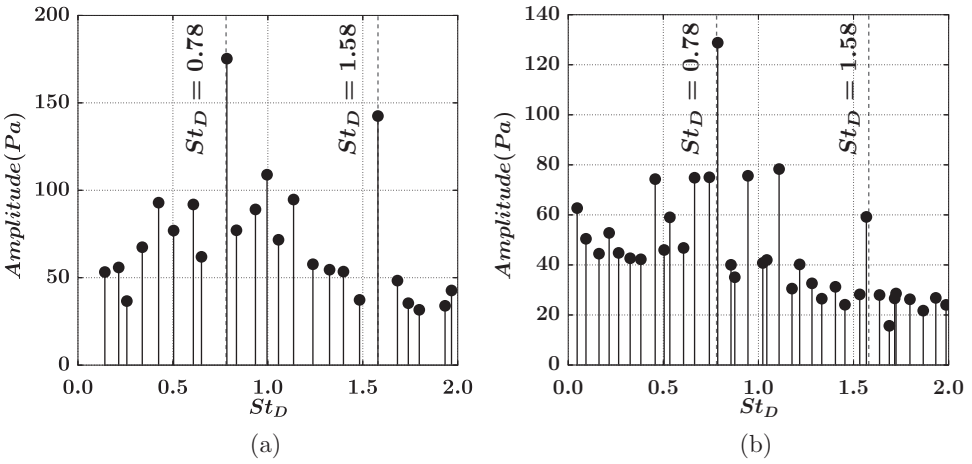

FIG. 19. The DMD amplitude spectra showing the area-weighted average amplitude of the pressure fluctuation in the $(y/D,z/D)$ plane as a function of the Strouhal number St_D for the (a) flat and (b) concave plates.

linked to the coherent structures resulting from pairing of the initial vortices generated by the roll-up of the shear layer. Therefore, these spectra seem to indicate that there is only one stage of pairing occurring for both flat and concave cases.

The spatial structure of mode 1, believed to be related to the initial instability of the shear layer, is first analyzed. Figure 20 shows the spatial representation of the real part of mode 1 $\mathrm{Re}[\Phi_1(\mathbf{x})]$ for both flat and concave plates. Mode 1 is active for both configurations in the shear layer of the free jet relatively close to the nozzle exit. This confirms that this high-frequency activity characterizes the initial instability of the shear layer. The spatial structure of mode 1 is symmetric with respect to the jet axis. This indicates that mode 1 is axisymmetric, i.e., the primary structures are coherent in the azimuthal direction. One can also note that this mode is a convective one as highlighted by the amplitude variations that are parallel to the main flow direction. The activity linked to mode 1 is also active near the wall but with an amplitude that is relatively small compared to mode 2 (see Fig. 21).

Finally, the spatial structure of mode 2 is also investigated in Fig. 21. This mode is related to the coherent structures, after one pairing stage, evolving close to the plate. The amplitude is relatively strong near the wall, indicating that it is a major contributor to the near-wall activity. Mode 2 is symmetric with respect to the jet axis, indicating that the coherent structures related to this mode

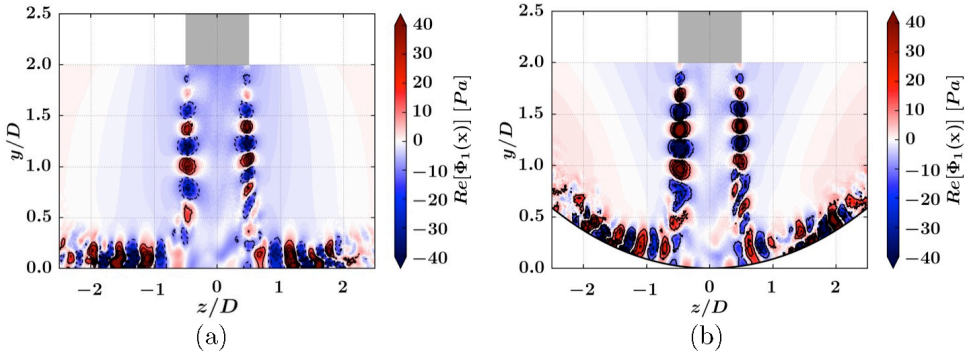

FIG. 20. Real part of mode 1 $\mathrm{Re}[\Phi_1(\mathbf{x})]$ at $\mathrm{St}_D = 1.58$ in the $(y/D,z/D)$ plane for the (a) flat and (b) concave plates.

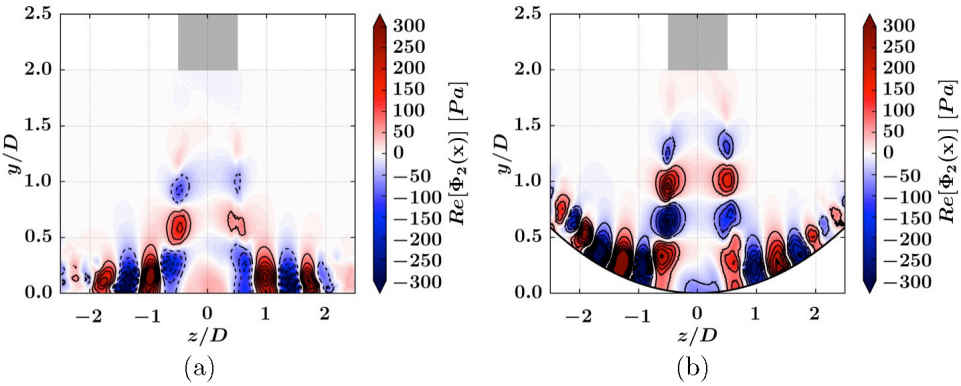

FIG. 21. Real part of mode $2\,\mathrm{Re}[\Phi_2(\mathbf{x})]$ at $\mathrm{St}_D = 0.78$ in the $(y/D,z/D)$ plane for the (a) flat and (b) concave plates.

are also coherent in the azimuthal direction. They are formed near $y/D \approx 1.0$ downstream of the region where the activity of mode 1 is more pronounced.

The investigations of the flow organization show very similar behavior between the flat and concave plates. The same instantaneous structures are observed in the free jet and wall jet regions. The modal analysis also shows that the same modes are present in the flow linked to the formation, interactions, and convection of the primary structures. In the present study, the concave curvature does not impact significantly the jet dynamics.

C. Wall imprint of coherent structures

1. Modal analysis

It is known that, at least for the flat plate, a relation exists between the development of the primary structures and the heat transfer at the wall [14,15]. Mode 2, identified in Sec. VI B 2, seems to drive the near-wall activity for both flat and concave configurations. To look at the wall imprint of the coherent structures, the DMD is also performed on the plates for the pressure signal. The resulting spectra are shown in Fig. 22 for both plates. The dominant mode identified on the plates corresponds to mode 2 detected in the flow.

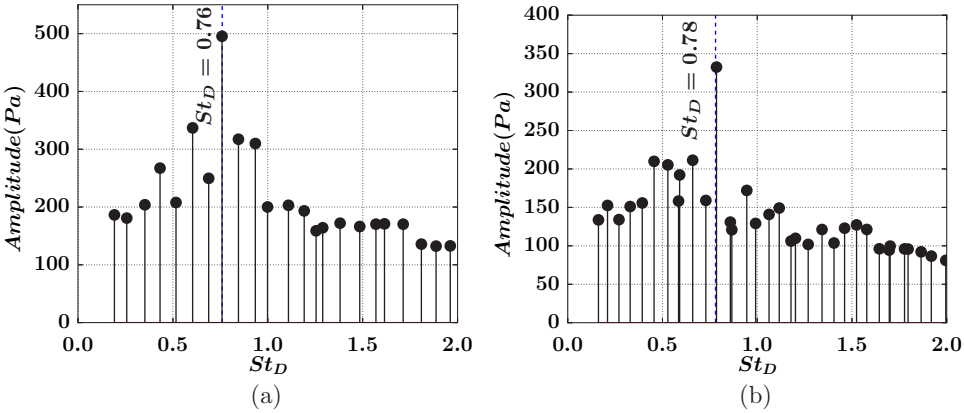

FIG. 22. The DMD amplitude spectra showing the area-weighted average amplitude of the pressure fluctuation on the plate as a function of the Strouhal number St_D for the (a) flat and (b) concave plates.

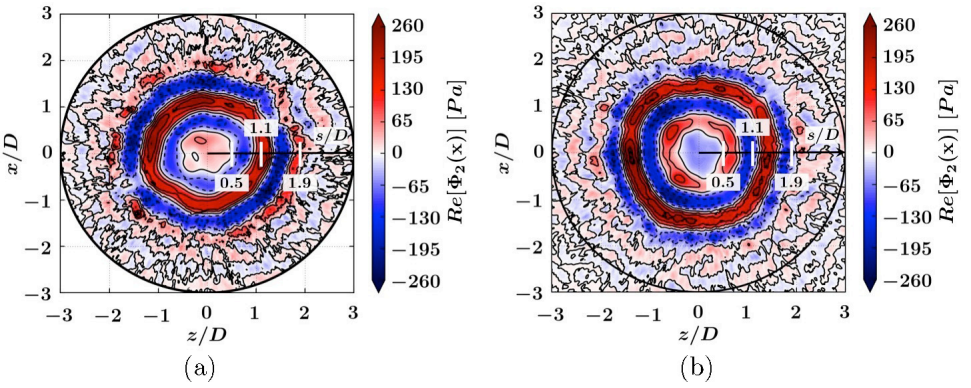

FIG. 23. Real part of mode 2 $\mathrm{Re}[\Phi_2(\mathbf{x})]$ at $\mathrm{St}_D \approx 0.78$ on the plate for the (a) flat and (b) concave plates.

This mode corresponds to the radial propagation of pressure fronts as shown in Fig. 23. It is directly linked to the passage of the primary and secondary structures. The activity is mainly concentrated in the region $1.1 < s/D < 1.9$ for the flat and concave plates. This region is correlated to the heat transfer enhancement leading to the occurrence of a secondary maximum in the mean-Nusselt number distribution for the flat plate case [16]. Further downstream, for $s/D > 1.9$, mode 2 loses its azimuthal coherence for both flat and concave surfaces. The loss of azimuthal coherence is closely related to the rebound of the primary structures at the end of the transition region (see Ref. [16]).

2. Unsteady behavior

It is known from the previous study of Didden and Ho [50] that the interaction between the primary structures and the wall induces an unsteady adverse pressure gradient. The unsteady behavior at the wall is evidenced in Fig. 24, showing the azimuthal average of the curvilinear pressure

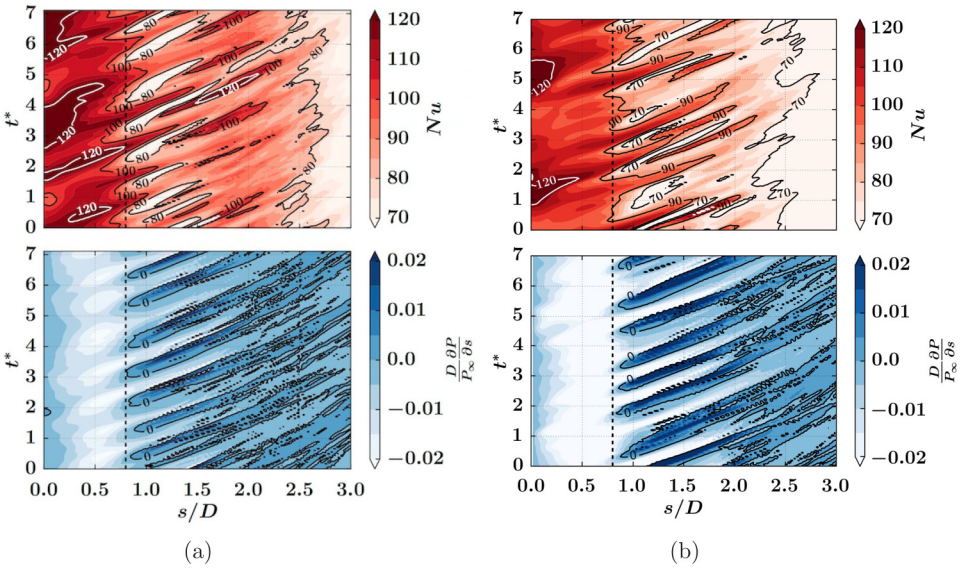

FIG. 24. Filled contours of the instantaneous azimuthally averaged Nusselt number Nu (top) and curvilinear pressure gradient $\partial P/\partial s$ (bottom) in the $(t^*, s/D)$ plane for the (a) flat and (b) concave plates. The dashed lines locate $s/D = 0.8$. Here t^* is the nondimensional time expressed as $t^* = t S_t U_b / D$, where $S_t = 0.78$.

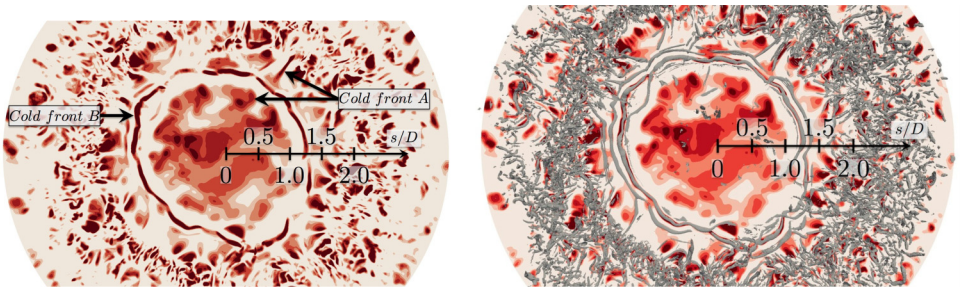

(a) (b)

FIG. 25. Snapshot of the Nusselt number Nu on (a) the flat plate identifying cold fronts A and B and (b) the secondary structures superimposed on cold front B. The scale for the Nusselt number goes from Nu = 70 (white) to Nu = 140 (red or black). The secondary structure is shown with an isosurface of the Q criterion $Q = 28U_b^2/D^2$ with a threshold applied showing only the part of the isosurface with a positive azimuthal vorticity.

gradient. For both cases, the wall imprint of the primary structures can be clearly seen with the quasiperiodic occurrence of an adverse pressure gradient, i.e., $\partial P/\partial s > 0$. The passage frequency equals approximately $\mathrm{St}_D = 0.78$, in agreement with the DMD results. The main effect of this adverse pressure gradient is to perturb intermittently the development of the wall jet and the convection of the cold fronts coming from the stagnation region (see Fig. 24). The adverse pressure gradient causes the unsteady separation of the boundary layer, which is reflected by the relatively small Nusselt number values Nu < 80 in Fig. 24(a). Then the separation evolves into a secondary structure that is responsible for the occurrence of relatively-high-Nusselt number values for the flat plate, Nu > 100 at $s/D \approx 1.25$, that do not come from the upstream stagnation region. This scenario observed for the flat plate is found also for the concave plate in Fig. 24(b). However, one can note that the high-Nusselt number events, caused by the secondary structures, have a lower intensity for the concave plate.

As shown in the previous study for the flat case [16] and in the spatiotemporal evolution of the Nusselt number in Fig. 24, two cold fronts are developing on the plate. These cold fronts are mainly driven by the interaction of the primary structures and the wall. Figure 25 shows these fronts along with the secondary structures. Cold front B has a strong azimuthal coherence and was found to be linked to the secondary structures as shown in Fig. 25(b). The other cold front, cold front A, is related to the development of the wall jet that is not perturbed by the primary structures. However, there is an influence of the streamwise structures on cold front A producing locally elongated Nusselt number patterns [see Fig. 25(a)].

Similar mechanisms are observed for the concave plate as shown in Figs. 26 and 27. It is possible to identify cold fronts A and B. As for the flat plate, cold front B is related to the secondary structure as shown by the superposition of the isosurface of the Q criterion in Fig. 26(b). A zoom in on the cold front A region for the concave plate, shown in Fig. 27, highlights the presence of elongated Nusselt number patterns that are intimately connected to the presence of the streamwise structures originating from the free jet instability. Note that such elongated patterns are also observed and connected to the streamwise structures for the flat plate case (not shown here). Nevertheless, the main point that should be emphasized is the presence of streamwise structures having an impact on the heat transfer at the wall and not related to a Görtler centrifugal instability. All patterns described above are found to be deterministic, i.e., repeatable, as can be seen in movie 1 (flat plate) [63] and movie 2 (concave plate) [63] available as Supplemental Material.

To summarize, the only significant difference is found for the intensity of cold front B generated by the secondary structures. It was shown previously that cold front B is caused by a modification of the near-wall mixing by the secondary structures [16]. In an attempt to explain the discrepancy between the flat and concave surfaces, this near-wall mixing is investigated in Sec. VI C 3.

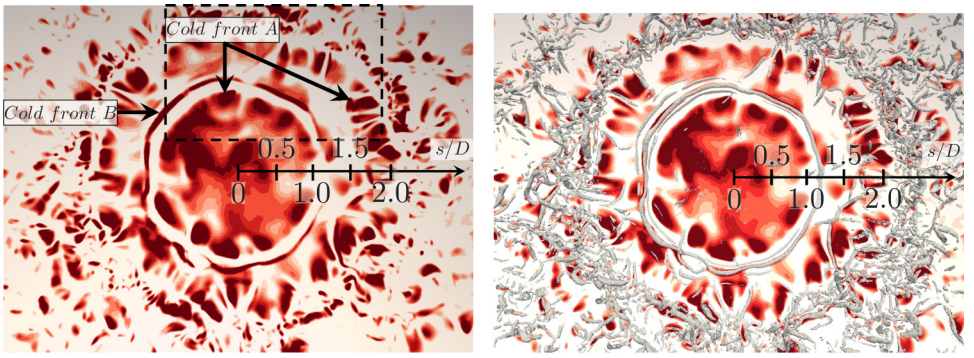

(a) (b)

FIG. 26. Snapshot of the Nusselt number Nu on (a) the concave plate identifying cold fronts A and B and (b) the secondary structures superimposed on cold front B. The scale for the Nusselt number goes from Nu $= 70$ (white) to Nu $= 120$ (red or black). The secondary structure is shown with an isosurface of the Q criterion $Q = 28U_b^2/D^2$ with a threshold applied showing only the part of the isosurface with a positive azimuthal vorticity.

3. Near-wall mixing

In the flat plate case, a cold fluid flux towards the wall produced by the secondary structures was evidenced using joint velocity-temperature probability density functions (PDFs) (see Ref. [16]). This was done using a quadrant analysis with numerical probes located on the secondary structures path at $n/D = 0.01$ and at ten different azimuthal positions. The quadrants are recalled in Fig. 28. They allow us to make the distinction between cold and hot fluid injection and ejection depending on the sign of the normal velocity component and the value of the temperature compared to the mean temperature. The cold fluid injections generated by the secondary structures are also present for the concave plate. To compare the intensity of these cold injection events for both plates, the conditional PDFs of the normal velocity U_n are built retaining only the events in quadrant Q_3. These

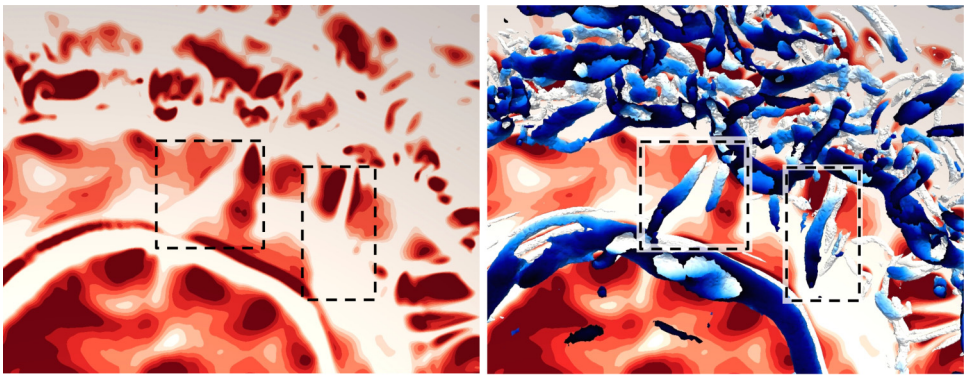

(a) (b)

FIG. 27. Zoom in on cold front A, dotted box in Fig. 26(a), showing (a) the instantaneous Nusselt number Nu and (b) the streamwise structures colored by the normal distance to the wall n/D. The scale for the Nusselt number goes from Nu $= 70$ (white) to Nu $= 120$ (red or black). The scale for the normal distance goes from $n/D = 0.04$ (white) to $n/D = 0.2$ (black). The streamwise structures are shown with an isosurface of the Q criterion $Q = 28U_b^2/D^2$.

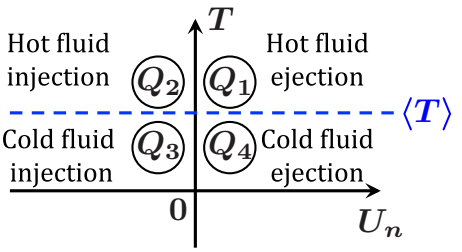

FIG. 28. Representation of the four quadrants in the (U_n, T) space. Injection and ejection events are identified, respectively, by $U_n < 0$ and $U_n > 0$. Hot and cold events are identified, respectively, by $T > \langle T \rangle$ and $T < \langle T \rangle$, where $\langle T \rangle$ is the time- and azimuthal-averaged local temperature.

conditional PDFs are shown in Fig. 29. According to the previous analyses and specifically to the spatiotemporal plot in Fig. 24, it is known that at $s/D = 1$ the secondary structure has not yet rolled up. Therefore, at this location the events are mainly concentrated near zero in the conditional PDF of U_n/U_b. At $s/D = 1.25$, the secondary structure has rolled up and it is possible to see the occurrence of relatively strong injection events for both flat and concave configurations. These strong events can also be seen further downstream as the secondary structures are convected along the plates. The comparison between the flat and concave plates highlights that strongest injection events are present for the flat case in the region where secondary structures are present. Hence, it seems that the concave curvature reduces the intensity of the cold fluid injections generated by the secondary structures. The alteration of the near-wall mixing could be the consequence of the stabilizing effect, existing in the outer layer of the wall jet [64], induced by the circular fluid motion on the concave plate.

D. Wall heat transfer: Statistical analysis

Similarities and differences between both flow configurations were highlighted in Secs. VI A–VI C. The aim is now to quantify from a statistical point of view the impact of the

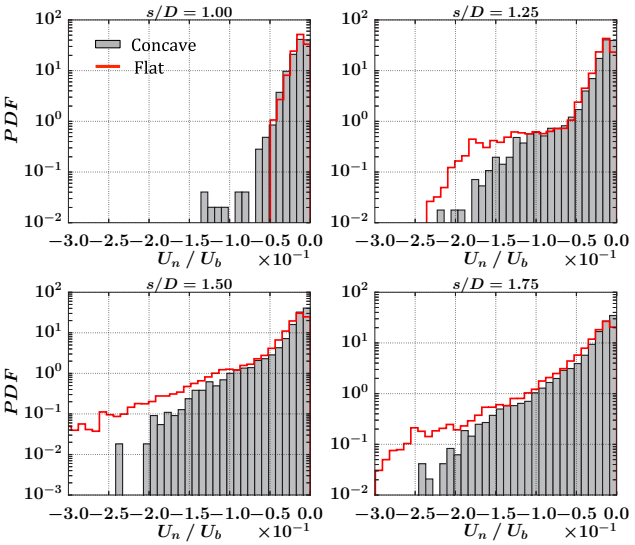

FIG. 29. Conditional PDFs of the normal velocity U_n retaining only the events in Q_3 (see Fig. 28) for the flat and concave plates for four positions s/D. The PDFs are obtained using numerical probes located at $n/D = 0.01$ at ten azimuthal positions.

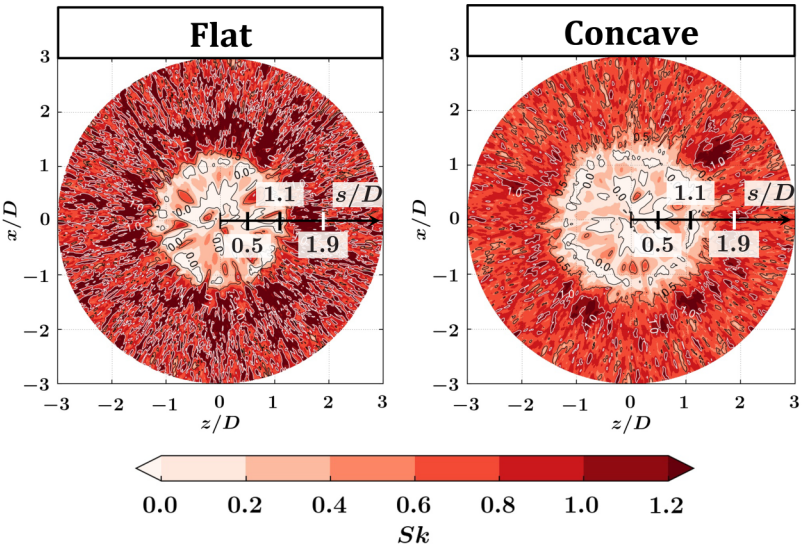

FIG. 30. Filled contours of the skewness Sk of the Nusselt number temporal distribution in the $(x/D,z/D)$ plane for the flat (left) and flattened concave (right) plates. Black isolines show $\mathrm{Sk} = 0$ and 0.5 and white isolines $\mathrm{Sk} = 1$.

plate curvature on the wall heat transfer. To do so, the nondimensional third-order central moment defined as $\langle [x(t) - \langle x(t) \rangle]^3 \rangle / \sigma^3$ is used, where $\langle \cdot \rangle$ denotes the time-averaging operator, $x(t)$ is the quantity of interest at one point of the computational domain, and σ is the standard deviation of the distribution. This odd central moment, called the skewness, evaluates the balance between the left and the right parts (with respect to the mean value) of a PDF. The skewness of a symmetric PDF, like a Gaussian distribution, is zero, but the reverse is not true. For a more detailed description of the meaning of this quantity in terms of the PDF and sample set, the reader is referred to the work of Tennekes and Lumley [65]. As the skewness is a high-order moment, i.e., third order, it is useful in the presence of intermittent events such as those related to the wall heat transfer time evolution for impinging jet flows.

Figure 30 presents the skewness of the Nusselt number temporal distribution for the flat and concave plates. Two remarkable locations can be identified. The first one is related to the generation of weak thermal events and appears as localized negative skewness values at several azimuthal locations at $s/D = 1.1$. These weak thermal events, not balanced by strong thermal events, are the results of the initiation of the unsteady separation of the boundary layer. They could be related to the temporal observation in Fig. 24, where the cold front A coming from the stagnation region is perturbed by the interaction between the primary structures and the plate. Further downstream, at $1.1 < s/D < 1.9$, the flat plate exhibits relatively-high-skewness values $\mathrm{Sk} > 1$ all along the azimuthal direction. This indicates the occurrence of extreme thermal events mainly due to the formation and convection of the secondary structures. Such regions of high skewness are also present for the concave plate but are less pronounced. The extreme thermal events generated by the secondary structures are less intense for the concave case, in agreement with previous observations in Sec. VI C.

To get an indication of the intensity of the different thermal events occurring at different spatial positions, the PDFs of the Nusselt number are provided in Fig. 31. First, the rapid decrease of the mean Nusselt number for $0.5 < s/D < 1.0$ is caused by the increased probability of occurrence of weak thermal events. The fall-off stops with the emergence of relatively strong thermal events as can be seen with the bump occurring for the flat plate. The relatively strong thermal events are also seen for the concave plate but with a lower intensity, agreeing with the previous analysis of the

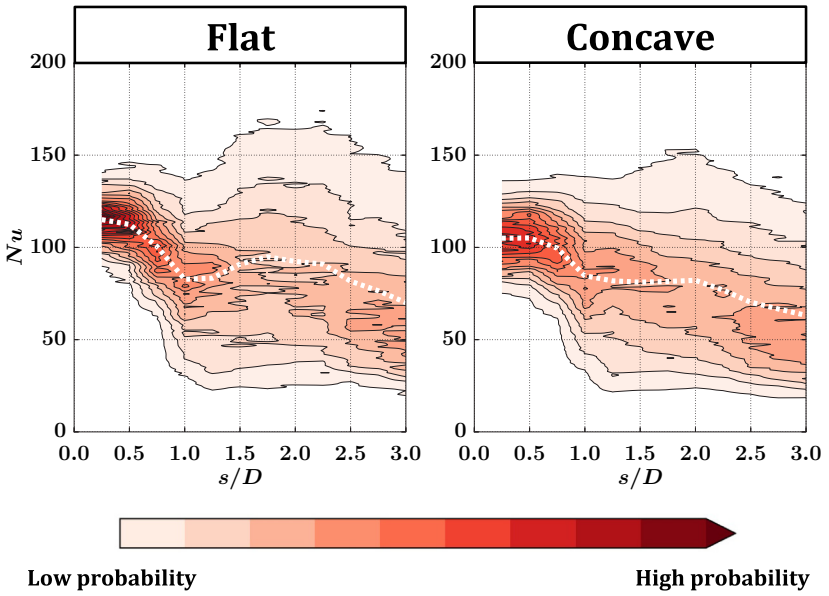

FIG. 31. The PDF of the Nusselt number Nu temporal distribution as a function of the distance to the stagnation point s/D for the flat (left) and concave (right) plates. The white dashed line shows the mean Nusselt number.

skewness on the plates. For the flat plate, the occurrence of these strong events creates an imbalance that pulls the mean towards higher-Nusselt number values and a secondary peak occurs. The strong events observed for the concave plate are not able to create such an imbalance and a plateau appears instead of a peak.

Finally, the mean Nusselt number is compared between the concave and flat plates in Fig. 32. The major discrepancy concerns the secondary peak found for the flat plate that is damped in the concave case as discussed above. The Nusselt number values are also lower in the stagnation region of the concave plate. The reduction is of the order of 8% in the stagnation region and 15% at the secondary peak location. For the configuration investigated here, the concave curvature is found to

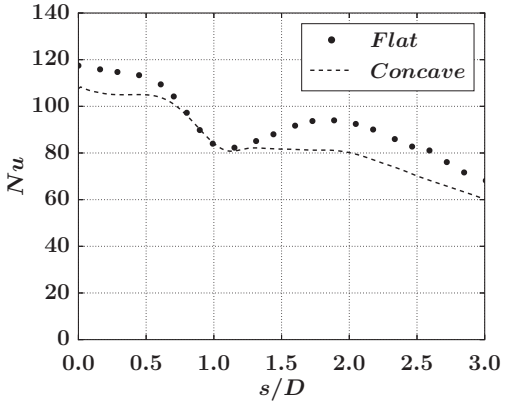

FIG. 32. Mean Nusselt number Nu as a function of the distance to the stagnation point s/D for the flat plate (•) and the concave plate (——).

decrease the heat transfer rate at the wall. At first sight, this observation is puzzling because current consensus tends to show that concave curvature has the ability to enhance the wall heat transfer due to the generation of Görtler structures caused by a centrifugal instability mechanism [66–69]. This statement is based on the necessary condition that Görtler vortices have to be present. It should be qualified by the fact that there is no evidence of the existence of these vortices in impinging jet flows. Therefore, a discussion is proposed in Sec. VII, presenting some arguments showing that heat transfer enhancement due to surface curvature for impinging jet flows is not as obvious. A possible explanation for the discrepancies observed in the literature is also proposed.

VII. DISCUSSION

Instabilities of flows over a concave surface have been studied for a long time. Several theoretical studies, confirmed by experimental investigations, have evidenced the development of coherent structures due to concave curvature [70]. The most common ones are found for relevant engineering flows such as flows between concentric rotating cylinders (Taylor vortices) [71], curved, fully developed channel flows (Dean vortices) [72], and boundary layer flows on concave walls (Görtler vortices) [73]. These coherent structures arise from the same physical mechanism linked to the presence of an unstable stratification of the centrifugal effect first described by Rayleigh for incompressible flows [74]. This centrifugal instability for rotating flows is caused by an inviscid mechanism originating essentially from the inability of the local pressure gradient to restrain the displacement of a fluid particle subject to a small perturbation. Rayleigh [74] showed that this inviscid mechanism is active when the so-called Rayleigh circulation criterion is satisfied,

$$\frac{\partial (ru)^2}{\partial r} < 0, \tag{6}$$

where r is the radial direction normal to the rotational axis oriented outward and u is the streamwise velocity component. This criterion is a necessary and sufficient condition for the existence of a centrifugal instability for inviscid flows.

Based on this knowledge, Sec. VII A focuses on the wall jet and the Görtler instability. In Sec. VII B, an investigation about the possibility to have a centrifugal instability in the deflection region is presented.

A. Wall jet

It is known that, for boundary layer flows, a region where $\partial (ru)^2/\partial r < 0$, i.e., where u decreases faster than $1/r$, exists [44]. For wall jets, Floryan [64] used an inviscid linear stability analysis to show that they behave differently from boundary layers. Indeed, a wall jet is composed of two layers. The inner layer extends from the wall to the location of the maximum streamwise velocity, while the outer layer goes from the location of the maximum velocity to the edge of the wall jet. Floryan [64] has shown that for a concave wall, the inner layer is inviscidly unstable, while the outer layer is inviscidly stable. This point is an important difference in distinguishing boundary layer and wall jet flows in terms of stability.

For real fluids, it is known that the viscosity has a stabilizing effect. Görtler [73] was the first to show, using a theoretical analysis, that the centrifugal instability appears for viscous boundary layer flows. This viscous instability modifies the basic flow by forcing fluid particles to go away from and toward the wall while preserving their basic-state velocity. Therefore, it manifests itself in the form of streamwise-oriented, counterrotating structures, known today as Görtler vortices. He has also shown that the critical parameter governing this viscous instability is the Görtler number defined as

$$\mathrm{Go} = \frac{U_s \delta}{\nu} \sqrt{\frac{\delta}{r_w}}, \tag{7}$$

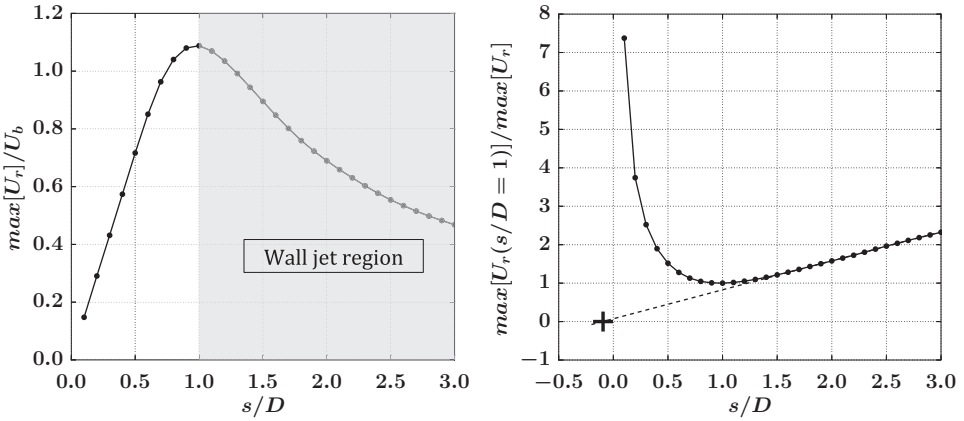

FIG. 33. (a) Maximum radial velocity in the wall region $\max[U_r]$ as a function of the curvilinear abscissa s/D. The shaded area represents the wall jet region. (b) Evolution of the inverse of the maximum radial velocity $\max[U_r(s/D=1)]/\max[Ur]$ as a function of the curvilinear abscissa s/D. The dots represent the location where the velocity profiles are extracted to find $\max[U_r]$. Also shown are the result of the linear regression to determine the virtual origin of the wall jet $(--)$ and the location of the virtual origin $(+)$.

where U_s is the appropriate velocity scale and $\delta = \sqrt{\nu x_0/U_s}$ is the appropriate thickness of the flow, with x_0 the characteristic length scale, ν the kinematic viscosity of the fluid, and r_w the radius of curvature of the wall. For a wall jet U_s is the maximum velocity and x_0 is distance to the virtual origin. This nondimensional number characterizes the ratio of inertial forces, taking into account the rotational motion, to the viscous forces. The results of Görtler [73] show that a threshold value exists for the Görtler number above which a small perturbation will be sustained or amplified. Floryan [64] extended the viscous theoretical analysis to wall jet flows. He was able to show that the presence of a stable region, for wall jets over concave surface, has a stabilizing effect compared to boundary layer flows as it adds additional dissipation. This leads to the delay of the transition compared to a boundary layer flowing over a concave surface, i.e., higher critical Görtler number.

As a wall jet exists in impinging jet flow, the present results can be compared to the theoretical results obtained by Floryan [64]. The wall jet region is considered here to start at the location where the maximum streamwise velocity $U_r = \mathbf{U} \cdot \mathbf{e}_\varphi$ is reached, i.e., $s/D = 1$ for the present configuration [see Fig. 33(a)]. To compute the Görtler number following the definition of Floryan [64], the virtual origin [39] of the wall jet needs to be determined. This is done by a linear regression in the region where the ratio $U_r(s/D=1)/\max(U_r)$ evolves linearly with respect to s/D as shown in Fig. 33(b). The resulting Görtler number in the wall jet region of the concave case is shown in Fig. 34(a) as a function of the curvilinear distance s/D. These results are compared to the theoretical findings of Floryan [64] in Fig. 34(b), showing the neutral stability curve obtained for a wall jet. The shaded area shows the possible values, for the wall jet studied here, in the (Go,α) plane, where α is the dimensionless azimuthal wave number. The range of azimuthal wave numbers is estimated from the biggest azimuthal wavelength that can exist in the domain and the smallest wavelength resolved on the grid. The smallest dimensionless wave number, proportional to the size of the computational domain, is of the order of 10^{-2} for the current simulation. The biggest resolved wave number is proportional to the grid resolution. Indeed, the upper limit is defined according to the Nyquist-Shannon criterion expressed as $\alpha < \pi/\Delta l$, where Δl is the characteristic length scale of the grid. As the wave number is normalized by δ [see Eq. (7)], it evolves along the curvilinear abscissa s/D. Therefore, the wave-number bounds of the shaded area in Fig. 34(b) are not vertical lines. Even with the restriction in terms of wave numbers, it appears that for the wall jet studied here a stable region exists. This shows that for the Görtler numbers obtained for this case, a range of perturbations

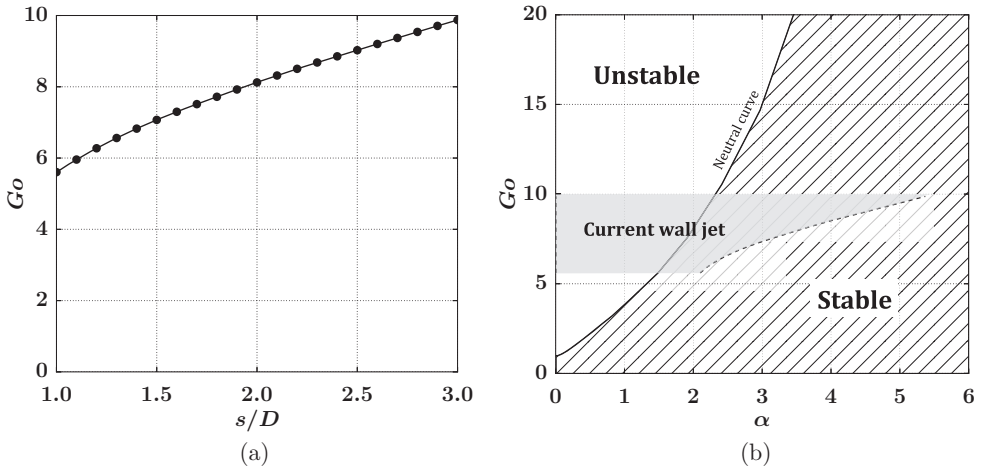

FIG. 34. (a) Görtler number Go in the wall jet region as a function of the curvilinear abscissa s/D. (b) Neutral stability curve obtained by Floryan [64] for a wall jet, where α is the spanwise or azimuthal wave number of the perturbation normalized by δ [see Eq. (7)]. The shaded area represents the Görtler number values found in the wall jet region for the jet impinging on the concave plate studied here.

exists that does not trigger the Görtler instability. On the other hand, it suggests that, when the wall jet starts at $s/D = 1$, the instability should be triggered for perturbations of dimensionless azimuthal wave number $\alpha < 1.5$. These specifics perturbations do not seem to be present in the current study as no Görtler vortices could be clearly evidenced.

It is also emphasized that the theoretical results of Floryan [64] deal with a laminar wall jet with zero pressure gradient. Strong pressure gradients exist in the impinging jet flow as revealed in Fig. 24. It has been shown recently that pressure gradients affect the Görtler instability for boundary layer flows [75]. Indeed, Rogenski *et al.* [75] have reported an alteration of the nonlinear development of Görtler vortices caused by an earlier saturation in the presence of an adverse pressure gradient (APG) compared to the zero pressure gradient case. On the other hand, a favorable pressure gradient (FPG) delays the saturation. In other words, the FPG has a stabilizing effect, while the APG has a destabilizing effect. For the impinging jet, it means that in the early development of the wall jet the existing steady FPG stabilizes the flow regarding the centrifugal instability mechanism, while the unsteady APG caused by the primary structure has a destabilizing effect. In addition to the importance of a pressure gradient, it should be recalled that the Görtler instability is weak, i.e., it has a small spatial amplification, and could be dominated by other types of instability such as the one related to the primary and secondary structures [76].

To conclude this part of the discussion, it is recalled that sometimes concave curvature is found to enhance heat transfer (see, e.g., Ref. [20]) and sometimes not (see Sec. VI D and Ref. [23]) even for a similar experimental setup (see the results of Lee *et al.* [24] leading to different conclusions about the curvature effect depending on the Reynolds number). One of the possible explanations for this discrepancy may be linked to the dependence of the Görtler instability on several parameters such as the Görtler number and the properties of the perturbation triggering the instability. One can note that the Görtler number is never reported in studies of an impinging jet on a curved surface. This makes it difficult to compare results coming from different studies. On the other hand, the perturbations are certainly present in all experimental setups and all numerical simulations, but are very difficult to characterize if not controlled. Perturbation with specific azimuthal wavelength could cause the wall jet to cross the neutral stability curve for a given Görtler number. This could explain the heat transfer enhancement observed in certain studies [20]. Hence, it would be interesting to investigate the response of an impinging jet flow on a concave surface to a controlled perturbation with a well

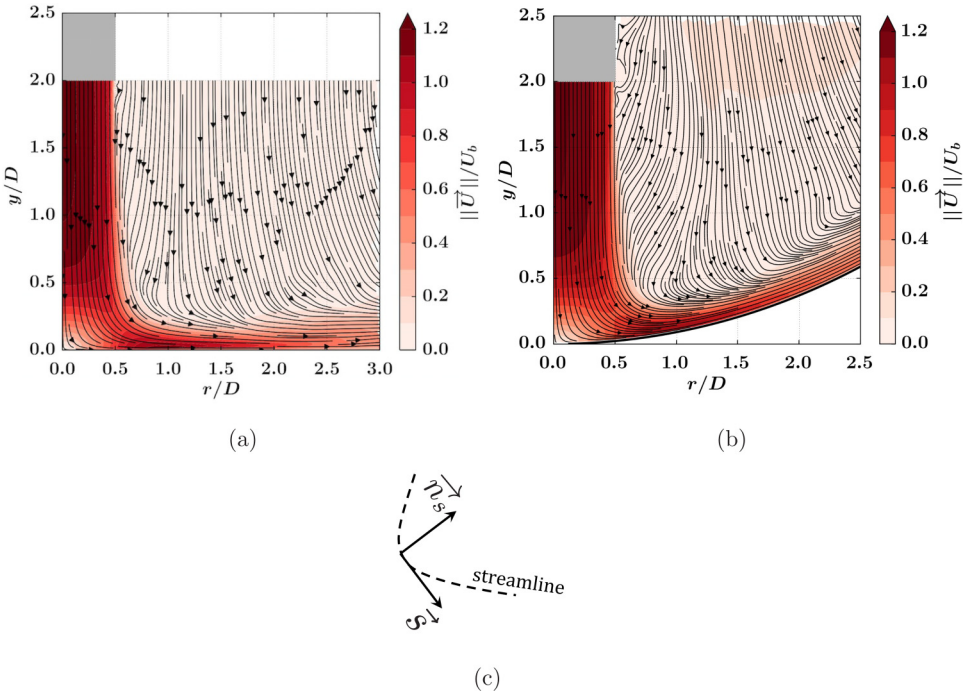

FIG. 35. Mean streamlines and filled isocontours of the normalized velocity magnitude $\|\vec{U}\|/U_b$ in the $(y/D,r/D)$ plane for the (a) flat and (b) concave plates. (c) Local coordinate system attached to a streamline.

defined azimuthal wave number. Moreover, it should be emphasized that heat transfer enhancement due to concave curvature is observed for a two-dimensional slot jet [20]. These slot jets resemble more the classical two-dimensional geometry for which Görtler instability was studied. In the case of axisymmetric config- urations, the radial expansion should be considered, as it will reduce the effect of Görtler vortices on the azimuthally averaged heat transfer.

B. Deflection region

The previous point relates to the known centrifugal instability for wall bounded flows over a concave surface. However, one has to recall that the biggest curvature for impinging jet flows is caused by the deflection of the jet due to the presence of the plate as highlighted in Fig. 35. To provide a quantitative evaluation of the importance of this deflection, the local curvature of the mean flow field can be evaluated and compared to the geometrical curvature of the concave plate. This is done by using the Euler equations written in a local coordinate system attached to a streamline. This local system is composed of a tangential $\vec{s}$ and a normal $\vec{n}_s$ unit vector as shown in Fig. 35(c). The projection on the normal unit vector $\vec{n}_s$ gives the relation defined in Eq. (8),

$$\frac{\rho u^2}{r_{\text{flow}}} = \frac{\partial P}{\partial n_s}, \tag{8}$$

where r_{flow} is the local radius of curvature of the flow and u is the velocity magnitude. The local radius of curvature r_{flow} is computed for both flat and concave plates and compared to the radius of curvature of the concave plate in Fig. 36. Note that the relative curvature for an impinging jet on curved surfaces is expressed in terms of diameter ratio, i.e., the ratio of the jet diameter D to the plate diameter d. Therefore, to be consistent with the initial notation, the comparison of the local radius of curvature and the radius of curvature of the plate is expressed as d/d_{flow}, where

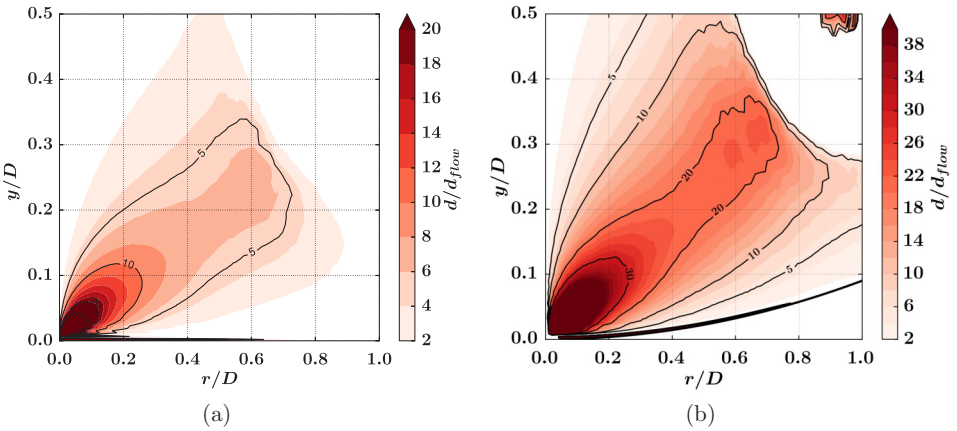

FIG. 36. Ratio of the concave plate radius of curvature to the local flow radius of curvature d/d_{flow} in the $(y/D,r/D)$ plane for the (a) flat and (b) concave plates.

$d_{\text{flow}} = 2r_{\text{flow}}$. This quantitative comparison allows us to see that the curvature of the plate is rather small compared to the curvature due to the flow deflection. For the flat plate, the curvature of the flow due to the deflection is of the order of 5 to 10 times greater than the concave plate curvature. For the concave case, the deflection is more pronounced and the flow curvature is found to be of the order of 20 to 30 times greater than the concave plate curvature. This points to the possibility of having a centrifugal instability in impinging jet flows, not only due to the plate curvature but also due to the flow deflection present for all impinging jet flow configurations, i.e., flat or curved plates. The first step to know if the flow is subject to a centrifugal instability is to look at the inviscid criterion. This point is addressed in Fig. 37, showing the values of the Rayleigh circulation criterion defined in Eq. (6). The Rayleigh instability criterion is satisfied, i.e., $\partial(ru)^2/\partial r < 0$, for both concave and flat plates in the flow deflection region. This indicates that the inviscid mechanism is active and could possibly lead to the occurrence of a viscous centrifugal instability. Nevertheless, these elements alone do not allow us to be fully conclusive about the stability of this region. Indeed, the stability criterion in the deflection region of a viscous impinging jet flow is not currently known.

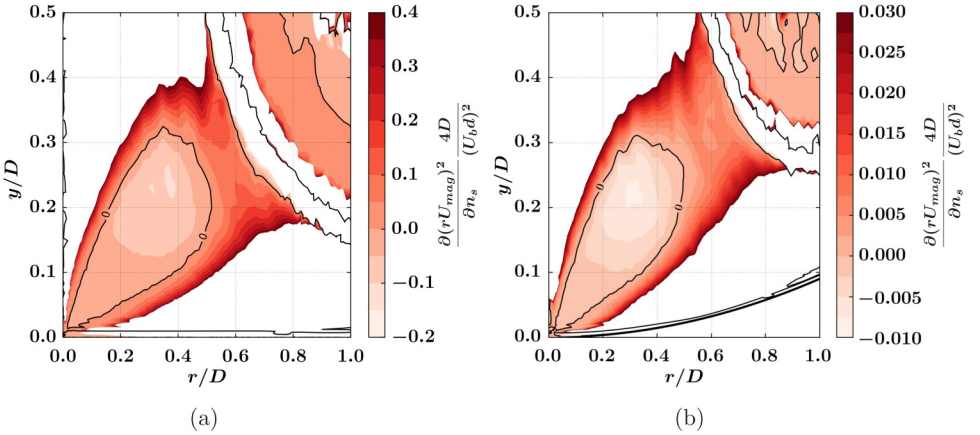

FIG. 37. Rayleigh circulation criterion in the $(y/D,r/D)$ plane for the (a) flat and (b) concave plates.

VIII. CONCLUSION

A wall-resolved LES of a single unconfined submerged axisymmetric air jet impinging on a hemispherical concave plate has been performed in an attempt to provide a detailed characterization of the surface curvature effect. The chosen operating point was a Reynolds number $\mathrm{Re} = 23\,000$ and a nozzle to plate distance $H/D = 2$. Numerical results were compared to the experimental data available in the literature and the main numerical uncertainty related to the method, that is the grid resolution, was assessed. As the main objective was to compare the present LES to a previous one for a flat plate impingement configuration, it was shown that the present results could be confidently used to characterize the surface curvature effect for both the flow dynamics and the heat transfer at the wall.

A detailed comparison between the flat and concave plates was reported. The mean development of both the free jet and the wall jet was found to be similar for both flat and concave cases. The same large-scale organization was highlighted for both configurations that contain the essential features present in such an impinging jet flow. The presence of streamwise vortices developing in the free jet, convected in the wall jet, and not related to a Görtler instability was reported for both flat and concave plates. The main differences observed in this study come from the near-wall mixing and the wall heat transfer. In the concave case, the secondary structures were found to produce less intense thermal events due to weaker cold fluid injections. This could be related to the stabilizing effect in the outer layer of the wall jet, induced by the circular fluid motion, as discussed in this paper. The evolution of the Nusselt number along the plate confirms these findings. Indeed, a reduction of the heat transfer at the wall is evidenced for the concave plate mainly due to a damped secondary peak. This result goes against the current consensus based on the legacy from boundary layer studies claiming that the concave curvature enhances the wall heat transfer due to the presence of Görtler vortices. Therefore, a discussion is proposed to shed light on some inherent features of impinging jet flows that should be considered prior to any analogy with boundary layer flows. According to theory, a wall jet over a concave surface is more stable than a boundary layer. Moreover, it is recalled that the wall jet can be stable depending on the Görtler number and the azimuthal wave number of the initial perturbation. In this study, no Görtler vortices could be clearly evidenced. In addition to the classical instability problem inherent to a curved wall, the deflection region was also shown to be inviscidly unstable due to the same centrifugal mechanism as the one operating for Görtler vortices. Finally, it is important to note that, compared to round jets, two-dimensional slot jets impinging on a cylindrical surface are more likely to exhibit heat transfer enhancement due to Görtler vortices as they are not subject to a radial expansion.

Regarding the results presented in this paper, a perspective could be a more in depth stability analysis of such an impinging jet flow, in particular in the deflection region identified as potentially unstable and where little is known in terms of stability.

ACKNOWLEDGMENTS

The authors acknowledge CINES of GENCI for giving access to HPC resources under Allocation No. 2017-x20172a6074. The authors are grateful to Safran Helicopter Engines for funding this work. Some of the postprocessing was performed using Antares [77] and the Antares team is gratefully acknowledged for providing the library and support.

[1] T. S. Lundgren, J. Yao, and N. N. Mansour, Microburst modeling and scaling, J. Fluid Mech. **239**, 461 (1992).

[2] U. Wählby, C. Skjölderbrand, and E. Junker, Impact of impingement on cooking time and food quality, J. Food Eng. **43**, 179 (2000).

[3] J.-C. Han and L. M. Wright, in *The Gas Turbine Handbook* (U.S. National Energy Technology Laboratory, Morgantown, 2007), p. 321.

[4] H. Martin, *Advances in Heat Transfer* (Elsevier, New York, 1977), Vol. 13.
[5] K. Jambunathan, E. Lai, M. A. Moss, and B. L. Button, A review of heat transfer data for single circular jet impingement, Int. J. Heat Fluid Flow **13**, 106 (1992).
[6] A. Dewan, R. Dutta, and B. Srinivasan, Recent trends in computation of turbulent jet impingement heat transfer, Heat Transfer Eng. **33**, 447 (2012).
[7] N. Zuckerman and N. Lior, Impingement heat transfer: Correlations and numerical modeling, J. Heat Transfer **127**, 544 (2005).
[8] C. O. Popiel and O. Trass, Visualization of a free and impinging round jet, Exp. Therm. Fluid Sci. **4**, 253 (1991).
[9] J. Vejrazka, J. Tihon, P. Marty, and V. Sobolík, Effect of an external excitation on the flow structure in a circular impinging jet, Phys. Fluids **17**, 105102 (2005).
[10] L. F. G. Geers, K. Hanjalic, and M. J. Tummers, Wall imprint of turbulent structures and heat transfer in multiple impinging jet arrays, J. Fluid Mech. **546**, 255 (2006).
[11] T. S. O'Donovan and D. B. Murray, Jet impingement heat transfer - Part II: A temporal investigation of heat transfer and local fluid velocities, Int. J. Heat Mass Transfer **50**, 3302 (2007).
[12] M. Hadžiabdić and K. Hanjalić, Vortical structures and heat transfer in a round impinging jet, J. Fluid Mech. **596**, 221 (2008).
[13] W. Rohlfs, H. D. Haustein, O. Garbrecht, and R. Kneer, Insights into the local heat transfer of a submerged impinging jet: Influence of local flow acceleration and vortex-wall interaction, Int. J. Heat Mass Transfer **55**, 7728 (2012).
[14] S. Roux, M. Fenot, G. Lalizel, L. E. Brizzi, and E. Dorignac, Evidence of flow vortex signatures on wall fluctuating temperature using unsteady infrared thermography for an acoustically forced impinging jet, Int. J. Heat Fluid Flow **50**, 38 (2014).
[15] T. Dairay, V. Fortuné, E. Lamballais, and L.-E. Brizzi, Direct numerical simulation of a turbulent jet impinging on a heated wall, J. Fluid Mech. **764**, 362 (2015).
[16] P. Aillaud, F. Duchaine, L. Y. M. Gicquel, and S. Didorally, Secondary peak in the Nusselt number distribution of impinging jet flows: A phenomenological analysis, Phys. Fluids **28**, 095110 (2016).
[17] P. Grenson, O. Léon, P. Reulet, and B. Aupoix, Investigation of an impinging heated jet for a small nozzle-to-plate distance and high Reynolds number: An extensive experimental approach, Int. J. Heat Mass Transfer **102**, 801 (2016).
[18] R. Viskanta, Heat transfer to impinging isothermal gas and flame jets, Exp. Therm. Fluid Sci. **6**, 111 (1993).
[19] D. E. Metzger, T. Yamashita, and C. W. Jenkins, Impingement cooling of concave surfaces with lines of circular air jets, J. Eng. Power **91**, 149 (1969).
[20] C. Gau and C. M. Chung, Surface curvature effect on slot-air-jet impingement cooling flow and heat transfer process, J. Heat Transfer **113**, 858 (1991).
[21] H. Thomann, Effect of streamwise wall curvature on heat transfer in a turbulent boundary layer, J. Fluid Mech. **33**, 283 (1968).
[22] C. Cornaro, A. S. Fleischer, and R. J. Goldstein, Flow visualization of a round jet impinging on cylindrical surfaces, Exp. Therm. Fluid Sci. **20**, 66 (1999).
[23] M. Fenot, E. Dorignac, and J. J. Vullierme, An experimental study on hot round jets impinging a concave surface, Int. J. Heat Fluid Flow **29**, 945 (2008).
[24] D. H. Lee, Y. S. Chung, and S. Y. Won, The effect of concave surface curvature on heat transfer from a fully developed round impinging jet, Int. J. Heat Mass Transfer **42**, 2489 (1999).
[25] F. Shum-Kivan, F. Duchaine, and L. Gicquel, *ASME Turbo Expo 2014: Turbine Technical Conference and Exposition* (ASME, Düsseldorf, 2014), paper GT2014-25152.
[26] N. Uddin, S. O. Neumann, and B. Weigand, LES simulations of an impinging jet: On the origin of the second peak in the Nusselt number distribution, Int. J. Heat Mass Transfer **57**, 356 (2013).
[27] A. Dauptain, B. Cuenot, and L. Y. M. Gicquel, Large eddy simulation of stable supersonic jet impinging on flat plate, AIAA J. **48**, 2325 (2010).
[28] R. J. Jefferson-Loveday and P. G. Tucker, LES of impingement heat transfer on a concave surface, Numer. Heat Transfer A **58**, 247 (2010).

[29] J. W. Baughn and S. Shimizu, Heat transfer measurements from a surface with uniform heat flux and an impinging jet, J. Heat Transfer **111**, 1096 (1989).
[30] M. Fenot, J. J. Vullierme, and E. Dorignac, Local heat transfer due to several configurations of circular air jets impinging on a flat plate with and without semi-confinement, Int. J. Therm. Sci. **44**, 665 (2005).
[31] T. Schönfeld and M. Rudgyard, Steady and unsteady flows simulations using the hybrid flow solver AVBP, AIAA J. **37**, 1378 (1999).
[32] L. Quartapelle and V. Selmin, in *Finite Elements in Fluids, Swansea* (Pineridge, Whiting, 1993), p. 1374.
[33] O. Colin and M. Rudgyard, Development of high-order Taylor-Galerkin schemes for LES, J. Comput. Phys. **162**, 338 (2000).
[34] J. Donea and A. Huerta, *Finite Element Methods for Flow Problems* (Wiley, New York, 2003).
[35] F. Duchaine, N. Maheu, V. Moureau, G. Balarac, and S. Moreau, Large-eddy simulation and conjugate heat transfer around a low-Mach turbine blade, J. Turbomach. **136**, 051015 (2013).
[36] D. Papadogiannis, F. Duchaine, L. Gicquel, G. Wang, and S. Moreau, Effects of subgrid scale modeling on the deterministic and stochastic turbulent energetic distribution in large-eddy simulations of a high-pressure turbine stage, J. Turbomach. **138**, 091005 (2016).
[37] L. Y. M. Gicquel, G. Staffelbach, and T. Poinsot, Large eddy simulations of gaseous flames in gas turbine combustion chambers, Prog. Energy Combust. Sci. **38**, 782 (2012).
[38] S. Mendez and F. Nicoud, Large-eddy simulation of a bi-periodic turbulent flow with effusion, J. Fluid Mech. **598**, 27 (2008).
[39] S. B. Pope, *Turbulent Flows* (Cambridge University Press, New York, 2000).
[40] F. Nicoud and F. Ducros, Subgrid-scale stress modeling based on the square of the velocity gradient tensor, Flow, Turbul. Combust. **62**, 183 (1999).
[41] D. R. Chapman and G. D. Kuhn, The limiting behavior of turbulence near a wall, J. Fluid Mech. **170**, 265 (1986).
[42] J. Smagorinsky, General circulation experiments with the primitive equations. I: The basics experiment, Mon. Weather Rev. **91**, 99 (1963).
[43] T. Poinsot and S. Lele, Boundary conditions for direct simulations of compressible viscous flows, J. Comput. Phys. **101**, 104 (1992).
[44] H. Schlichting, in *Boundary-Layer Theory*, 7th ed., edited by F. J. Cerra (McGraw-Hill, New York, 1979).
[45] D. Cooper, D. C. Jackson, B. E. Launder, and G. X. Liao, Impinging jet studies for turbulence model assessment Part I. Flow field experiments, Int. J. Heat Mass Transfer **36**, 2675 (1993).
[46] N. Guezennec and T. Poinsot, Acoustically nonreflecting and reflecting boundary conditions for vorticity injection in compressible solvers, AIAA J. **47**, 1709 (2009).
[47] V. Granet, O. Vermorel, T. Leonard, L. Gicquel, and T. Poinsot, Comparison of nonreflecting outlet boundary conditions for compressible solvers on unstructured grids, AIAA J. **48**, 2348 (2010).
[48] P. Sagaut, *Large Eddy Simulation for Incompressible Flows* (Springer, Berlin, 2000).
[49] M. Bovo and L. Davidson, Direct comparison of LES and experiment of a single-pulse impinging jet, Int. J. Heat Mass Transfer **88**, 102 (2015).
[50] N. Didden and C.-M. Ho, Unsteady separation in a boundary layer produced by an impinging jet, J. Fluid Mech. **160**, 235 (1985).
[51] D. Liepmann and M. Gharib, The role of streamwise vorticity in the near-field entrainment of round jets, J. Fluid Mech. **245**, 643 (1992).
[52] A. Dazin, P. Dupont, and M. Stanislas, Experimental characterization of the instability of the vortex ring. Part II: Non-linear phase, Exp. Fluids **41**, 401 (2006).
[53] M. Bergdorf, P. Koumoutsakos, and A. Leonard, Direct numerical simulations of vortex rings at $\mathrm{Re}\Gamma = 7500$, J. Fluid Mech. **581**, 495 (2007).
[54] R. Örlü and P. H. Alfredsson, The life of a vortex in an axisymmetric jet, J. Visual. **14**, 5 (2011).
[55] K. P. Lynch and B. S. Thurow, 3-D flow visualization of axisymmetric jets at Reynolds number 6,700 and 10,200, J. Visual. **15**, 309 (2012).
[56] A. K. M. F. Hussain, Coherent structures and turbulence, J. Fluid Mech. **173**, 303 (1986).
[57] L. P. Bernal and A. Roshko, Streamwise vortex structure in plane mixing layers, J. Fluid Mech. **170**, 499 (1986).

[58] J. Jeong and F. Hussain, On the identification of a vortex, J. Fluid Mech. **285**, 69 (1995).
[59] S. E. Widnall and J. P. Sullivan, On the stability of vortex rings, Proc. R. Soc. London Ser. A **332**, 335 (1973).
[60] P. G. Saffman, The number of waves on unstable vortex rings, J. Fluid Mech. **84**, 625 (1978).
[61] J. Jimenez, A spanwise structure in the plane shear layer, J. Fluid Mech. **132**, 319 (1983).
[62] P. J. Schmid, Dynamic mode decomposition of numerical and experimental data, J. Fluid Mech. **656**, 5 (2010).
[63] See Supplemental Material at http://link.aps.org/supplemental/10.1103/PhysRevFluids.2.114608 for the instantaneous evolution of the Nusselt number on the flat plate and the concave plate.
[64] J. M. Floryan, Görtler instability of boundary layers over concave and convex walls, Phys. Fluids **29**, 2380 (1986).
[65] H. Tennekes and J. L. Lumley, *A First Course in Turbulence* (MIT Press, Cambridge, 1972).
[66] P. D. McCormack, H. Welker, and M. Kelleher, Taylor-Goertler vortices and their effect on heat transfer, J. Heat Transfer **92**, 101 (1970).
[67] J. T. C. Liu and A. S. Sabry, Concentration and heat transfer in nonlinear Gortler vortex flow and the analogy with longitudinal momentum transfer, Proc. R. Soc. A **432**, 1 (1991).
[68] R. Toe, A. Ajakh, and H. Peerhossaini, Heat transfer enhancement by Görtler instability, Int. J. Heat Fluid Flow **23**, 194 (2002).
[69] L. Momayez, P. Dupont, and H. Peerhossaini, Some unexpected effects of wavelength and perturbation instability strength on heat transfer enhancement by Görtler instability, Int. J. Heat Mass Transfer **47**, 3783 (2004).
[70] W. S. Saric, Görtler vortices, Annu. Rev. Fluid Mech. **26**, 379 (1994).
[71] G. I. Taylor, Stability of a viscous liquid contained between two rotating cylinders, Philos. Trans. R. Soc. London Ser. A **223**, 289 (1923).
[72] W. R. Dean, Fluid motion in a curved channel, Proc. R. Soc. London Ser. A **121**, 402 (1928).
[73] H. Görtler, On the three-dimensional instability of laminar boundary layers on concave walls, NACA report, 1940 (unpublished).
[74] Lord Rayleigh, On the dynamics of revolving fluids, Philos. Trans. R. Soc. London Ser. A **93**, 148 (1917).
[75] J. K. Rogenski, L. F. De Souza, and J. M. Floryan, Non-linear aspects of Görtler instability in boundary layers with pressure gradient, Phys. Fluids **28**, 124107 (2016).
[76] J. M. Floryan, On the Görtler instability of boundary layers, Prog. Aerosp. Sci. **28**, 235 (1991).
[77] Antares: pre-, post-, and co-processing library: http://cerfacs.fr/antares/.